MIT Open Access Articles

Combinatorial patterns of graded RhoA activation and uniform F-actin depletion promote tissue curvature

1

Combinatorial patterns of graded RhoA activation and uniform F-actin depletion

promote tissue curvature

4

Marlis Denk-Lobnig[1], Natalie C Heer[1], Adam C Martin[1, 2]

6

[1] Biology Department, Massachusetts Institute of Technology, 77 Massachusetts Ave.,

Cambridge, MA 02139

[2] Corresponding author: acmartin@mit.edu

10   **Abstract**

11   During development, gene expression regulates cell mechanics and shape to sculpt tissues.

12   One example is epithelial folding, which proceeds through distinct cell shape changes that

13   occur in different regions of the tissue. How transcription factors combinatorially coordinate

14   cell shape across a tissue is poorly understood. Here, using *Drosophila melanogaster* as a

15   model, we investigate how cell shape changes are coordinated to promote tissue bending

16   during gastrulation. By quantifying the multicellular patterns of RhoA activation, F-actin, and

17   myosin-2 and perturbing RhoA activation, we find that Snail and Twist regulate distinct

18   patterns of graded F-actin accumulation and uniform F-actin depletion, which synergize to

19   create zones of high and low F-actin levels within the *Drosophila* mesoderm. Graded

20   actomyosin results from a gradient in RhoA activation and the width of this zone regulates

21   tissue curvature. Thus, changes in tissue shape are regulated through the choreographed

22   interplay of distinct gene expression patterns.

Introduction

23   During development, the three-dimensional shape of a complex organism is generated

25   based on patterning that is encoded by the one-dimensional sequence of nucleotides in the

26   genome. Patterns of gene expression, and resulting signaling processes, overlap and

27   interact in space and time to define each cell's function. For example, morphogen gradients

28   encode positional information for specific cell fates (Rogers and Schier, 2011; Wolpert,

29   1969). For tissues to obtain their final shape and functional state, not only do cell fates need

30   to be positionally specified, but also cell shapes and mechanical properties; mechanical

31   properties and force generation are often patterned within a group of cells of the same fate

32   (Mongera et al., 2018; Sui et al., 2018; Sumigray et al., 2018). Each tissue shape change

33   requires coordinated changes in cell shape and position across the tissue, which have to be

34   tailored to the tissue's morphological and functional requirements while exhibiting robustness

35   and reproducibility between individual embryos/organisms (Chanet et al., 2017; Hong et al.,

36   2016; von Dassow and Davidson, 2009).

37   Mesoderm invagination in the early *Drosophila melanogaster* embryo is an

38   established model system for gene expression patterning and morphogenesis (Leptin,

39   2005). This system is powerful to study tissue folding because of its relative simplicity; in this

40   process, a single epithelial sheet at the surface of the embryo folds, driven by geometric

41   shape change of non-dividing cells (i.e., the number of cells is constant). Mesoderm

42   invagination requires apical constriction, a cell shape change driven by actomyosin

43   contraction that converts columnar epithelial cells to a wedge shape and promotes tissue

44   curvature (Leptin and Grunewald, 1990; Sweeton et al., 1991). Importantly, apical

45   constriction is coordinated across the presumptive mesoderm; there is a spatial, ventral-

46   lateral gradient of apical non-muscle Myosin-2 (myosin) and apical constriction that is

47   centered within the mesoderm (Heer et al., 2017; Lim et al., 2017; Spahn and Reuter, 2013)

48   (Figure 1 A). A zone of maximal apical constriction extends from the ventral midline up to 2

49   cell diameters on each side, while apical constriction beyond cell row 2 gradually declines up

50   to 5 cells from the midline (Heer et al., 2017). At the border of this gradient, about 2 - 4

51   lateral cell rows (row ~ 6 – 9) stretch their apical surface and bend toward the forming furrow

52   (Heer et al., 2017; Leptin and Grunewald, 1990; Sweeton et al., 1991). In contrast, more

53   lateral cells, which are part of the neighboring ectoderm, maintain almost constant apical

54   area throughout the folding process (Rauzi et al., 2015). We investigated how this tissue-

55   wide pattern of cell shape is established and its relevance to achieving proper tissue shape.

56   Mesoderm cell shape change and cell fate are initiated by the transcription factors

57   Twist and Snail, which exhibit distinct patterns of expression (Boulay et al., 1987; Furlong et

58   al., 2001; Leptin, 1991; Thisse et al., 1988). In the early syncytial blastoderm, *twist* mRNA is

59   expressed in a narrow band along the anterior-posterior axis on the ventral side of the

60   embryo, which expands dorsally into a wider band at the cellular blastoderm stage (Leptin,

61   1991). Measurements of the transcription dynamics of Twist target genes, *T48* and *fog*,

62   demonstrate that downstream Twist targets are expressed first at the ventral midline and

63   also expand laterally (Lim et al., 2017). This temporal progression of gene expression results

64   in the graded accumulation of T48 transcripts and protein along the ventral-lateral axis (Heer

65   et al., 2017; Lim et al., 2017; Rahimi et al., 2019). Snail can both activate and repress gene

66   expression (Rembold et al., 2014). One gene that is activated by Snail is the G-protein

67   coupled receptor (GPCR), Mist (Manning et al., 2013). In contrast to graded Twist activity,

68   Snail activity as assessed by Mist mRNA expression is uniform across the mesoderm (Lim et

69   al., 2017). Furthermore, Snail expression exhibits a sharp boundary between mesoderm and

70   ectoderm, whereas Twist expression is graded, extending up to ~2-3 cells across this

71   boundary into the ectoderm (Leptin, 1991). How these overlapping but distinct expression

72   patterns combinatorially contribute to cell shape change across the tissue is not understood.

73   The Twist target gene Fog activates the Mist GPCR and a uniformly expressed

74   GPCR, Smog (Costa et al., 1994; Kerridge et al., 2016; Manning et al., 2013). This GPCR

75   pathway, in parallel with T48 expression, results in apical myosin activation (Kolsch et al.,

76   2007). The GPCR pathway and T48 act via the guanine nucleotide exchange factor (GEF)

77   RhoGEF2, which activates RhoA (Barrett et al., 1997; Hacker and Perrimon, 1998).

78   Functioning in opposition to RhoGEF2 is the RhoA GTPase-activating protein (GAP) C-GAP

79   (Cumberland-GAP or RhoGAP71E) (Mason et al., 2016). RhoA coordinately activates

80   myosin via Rho-associated and coiled coil kinase (ROCK), and F-actin assembly via the

81   formin Diaphanous (Dawes-Hoang et al., 2005; Homem and Peifer, 2008). Myosin activation

82   occurs in a gradient that is narrower than the mid-cellularization gradient of Twist mRNA

83   accumulation (Heer et al., 2017). How the Twist activity pattern translates to RhoA activation

84   and how RhoA controls the tissue-wide pattern of actomyosin are not known.

85   During apical constriction, F-actin is apically enriched in ventral cells and proper F-

86   actin organization depends on RhoA signaling (Fox and Peifer, 2007). Conversely,

87   upregulation of F-actin turnover and decreased F-actin levels have been shown in the

88   mesoderm, which allows dynamic actomyosin network reattachment to junctions during

89   constriction (Jodoin et al., 2015). How F-actin is regulated across the mesoderm tissue and

90   how this is associated with patterned myosin and cell shape change are not understood.

91   Here we show that the tissue-level pattern of F-actin levels is distinct from myosin

92   activation and Twist activity. Snail activity uniformly depletes F-actin across the mesoderm.

93   Graded Twist activity promotes an actomyosin gradient within the zone of F-actin depletion,

94   creating distinct zones of constriction and stretching. We show that the width of this

95   actomyosin gradient is tuned by the activity of the RhoA pathway, which regulates tissue

96   curvature and lumen size in the mesodermal tube structure that results from this fold. Our

97   results show how the combination of overlapping transcriptional pre-patterns coordinates cell

98   shapes across the mesoderm to promote proper tissue curvature.

99   **Results**

100   **Myosin and F-actin exhibit distinct tissue-level patterns during mesoderm**

101   **invagination**

102   Apical myosin activation occurs in a multicellular gradient around the ventral midline (Figure

103   1 A) (Heer et al., 2017; Lim et al., 2017; Spahn and Reuter, 2013). However, how F-actin is

104   patterned is unknown. To determine the distribution of F-actin levels during mesoderm

105   invagination, we stained embryos with labeled phalloidin and measured cortical F-actin

106   levels by cell row, similarly to how we had measured multicellular patterns of myosin (Heer

107   et al., 2017). This method involved binning cells at different positions from the ventral midline

108   in order to obtain an average protein signal per cell at a given position along the ventral-

109   lateral axis. In contrast to myosin, for which the activated pool accumulates at the apical

110   surface, F-actin (as detected by phalloidin) is most apparent at intercellular junctions.

111   Junctional F-actin levels were higher in the ectoderm than the neighboring mesoderm cells

112   during ventral furrow formation (Jodoin et al., 2015). The difference in F-actin levels between

113   mesoderm and ectoderm was already present before ventral furrow initiation: there was a

114   clear boundary between low (mesoderm) and high (ectoderm) F-actin concentration zones

115   starting at mid-late cellularization, before apical constriction had started (Figure 1 B and D

116   and Supplement to Figure 1 A). During ventral furrow formation, junctional F-actin at the

117   center of the mesoderm increased to form a gradient that extended from cell 2 to cell 6,

118   similar to apical myosin (Figure 1 C and D).

119   The result of F-actin accumulation in ventral midline cells and persistent F-actin

120   depletion in marginal mesoderm cells was a zone of junctional F-actin depletion in cell rows

121   ~ 6 - 9 of the mesoderm and a discrete boundary between mesoderm and ectoderm (Figure

122   1C), forming a pattern distinct from that of myosin (Figure 1A). This pattern was also

123   observed in live embryos expressing the actin-binding domain of utrophin fused to green

124   fluorescent protein (Utrophin::GFP) or mCherry (Utrophin::mCherry), but not with a general

125   membrane marker, Gap43-mCherry, indicating that this measurement is not a fixation

126   artifact or due to changes in plasma membrane structure (Supplement to Figure 1 B). The

127   lower levels of F-actin were not as striking in Utrophin::GFP as in phalloidin-stained

128   embryos, likely because Utrophin interferes with F-actin remodeling (Spracklen et al., 2014);

129   however, we were able to reproducibly detect differences between mesoderm and ectoderm.

130   The observed tissue-wide pattern of F-actin was strikingly similar to the pattern of

131   apical constriction and stretching. Cell rows that maintained low F-actin levels were the

132   same cell rows at the margin of the mesoderm that stretched during folding (Figure 1 A, C).

133   This led us to hypothesize that F-actin levels could influence cell mechanics and the ability to

134   stretch under stress, which has been shown in other contexts (Salbreux et al., 2012; Stricker

135   et al., 2010). To test the strength of this relationship, we plotted the average cell junctional F-

136   actin intensity as a function of apical cell area for both mesoderm and adjacent ectoderm

137   cells (Figure 1 E). We found that F-actin levels were anti-correlated with cross-sectional

138   apical area. In summary, unlike apical myosin, junctional F-actin exhibited a clear difference

139   between mesoderm and ectoderm, which could explain why lateral mesoderm cells stretch

140   while neighboring ectoderm cells maintain their apical area during tissue folding.

141

142   **Snail and Twist regulate distinct components of the F-actin pattern**

143   To determine whether patterned gene expression regulates F-actin across the mesoderm,

144   we tested how the transcription factors *snail* and *twist* affect the tissue-level pattern of F-

145   actin levels. Snail activity in the mesoderm, as measured by *mist* transcription, is uniform

146   (Lim et al., 2017). We found that the Snail expression boundary co-localized precisely with

147   the boundary in F-actin depletion (Figure 2 A). Therefore, Snail expression and cortical F-

148   actin depletion are correlated.

149   Next, we determined whether cortical F-actin depletion is dependent on *snail.* Unlike

150   control (heterozygous) embryos, *snail* homozygous mutant embryos expressing

151   Utrophin::GFP did not exhibit patterned cortical F-actin levels in the ventral region (Figure 2

152   B). Quantification of subapical F-actin levels across the ventral and ventral-lateral domain in

153   *snail* mutants revealed no boundary, but uniform intensity throughout the region (Figure 2 C).

154   In addition, *snail* mutants lacked the ventral gradient in F-actin accumulation, consistent with

155   Snail being required for downstream effects of Twist, such as apical myosin activation and

156   dynamics (Kolsch et al., 2007; Martin et al., 2009). Because *snail* mutant embryos were

157   imaged live, we were able to confirm that we were examining ventral cells based on

158   germband extension movements in the neighboring ectoderm and premature cell divisions

159   that occurred in the uninternalized mesoderm, which is mitotic domain 10 (Foe, 1989;

160   Grosshans and Wieschaus, 2000). Therefore, Snail promotes uniform F-actin depletion

161   across mesoderm cells prior to gastrulation.

162   In contrast to Snail, the pattern of Twist activity across the mesoderm temporally

163   evolves, with Twist targets initiating first along the ventral midline and then expanding

164   laterally, which results in a gradient of accumulated transcripts (Lim et al., 2017; Rahimi et

165   al., 2019). To determine the effects of *twist,* we examined F-actin levels in a *twist* null mutant

166   that has been shown to disrupt myosin stabilization (Martin et al., 2009). In contrast to *snail*

167   mutants, *twist* mutant embryos exhibited F-actin depletion in the mesoderm and a clear

168   boundary to more lateral tissue with higher F-actin levels (Figure 2 D, E). The zone of F-actin

169   depletion was decreased to about half the normal width, consistent with previous studies

170   showing that *twist* mutants reduce the width of *snail* expression (Leptin, 1991). However,

171   graded F-actin accumulation around the ventral midline was absent in *twist* mutants,

172   suggesting that it specifically depends on the Twist pathway, which includes RhoA

173   activation. Therefore, mesodermal control of F-actin by Twist and Snail is comprised of two

174   nested layers: 1) prior to ventral furrow formation, uniform Snail activity depletes F-actin

175   across the mesoderm, and 2) during ventral furrow formation, graded Twist activity increases

176   F-actin accumulation in a ventral-lateral gradient (similar to apical myosin), but marginal

177   mesoderm cells maintain lower cortical F-actin.

178

179   **RhoA activation occurs in a gradient**

180   We next investigated how the gradient in Twist activity is transduced into a gradient of

181   actomyosin. Fog and T48 transcripts accumulate in a gradient (Lim et al., 2017; Rahimi et

182   al., 2019), but how downstream RhoA activation is patterned was not known. Fluorescently

183   tagged versions of RhoA's activator RhoGEF2 (under an endogenous promoter, Figure 3 B),

184   the Anillin Rho-binding domain, an active RhoA sensor (Figure 3 D), and the RhoA effector

185   ROCK (Figure 3 F) became apically enriched in ventral cells during ventral furrow formation,

186   consistent with previous studies (Kolsch et al., 2007; Mason et al., 2013; Mason et al.,

187   2016). Quantification of apical fluorescence by cell row revealed that all three markers for

188   RhoA pathway activation were graded along the ventral-lateral axis, exhibiting strong

189   fluorescence at the ventral midline and gradually decreasing to baseline after 5 cells (Figure

190   3 C, E, and G). In contrast, endogenously tagged C-GAP-GFP was largely cytoplasmic and

191   appeared uniform across the ventral domain during folding (Supplement to Figure 3 A).

192   The width of the gradient in RhoA activation, about 5 cells from the ventral midline, is

193   narrower than that of Twist mRNA, which extends 10-12 cells from the ventral midline (Heer

194   et al., 2017). Thus, RhoA activation occurs in a gradient, but the gradient does not mirror

195   Twist activity, suggesting that additional factors may modulate the downstream activity of the

196   Twist pathway.

197

198   **Neither graded myosin activation nor F-actin depletion depend on intercellular**

199   **mechanical connections**

200   Our data suggests that Snail and Twist promote uniform mesodermal F-actin depletion prior

201   to apical constriction and subsequent graded actomyosin activation within the mesoderm

202   during furrow formation, respectively. In the ventral furrow and the related process of

203   *Drosophila* posterior midgut formation, it has been proposed that mechanical feedback

204   between constricting cells is required to induce myosin accumulation, which may contribute

205   to a gradient or wave in contractility (Bailles et al., 2019; Mitrossilis et al., 2017). Therefore, it

206   was possible that mechanical induction of myosin also contributes to the gradient.

207   To determine the contributions of mechanical induction to multicellular patterns of

208   myosin activation and cortical F-actin levels, we examined embryos in which intercellular

209   cytoskeletal coupling was disrupted. We did this by depleting the adherens junction protein

210   α-catenin by RNA interference (α-catenin-RNAi). α-catenin-RNAi has been shown to

211   dramatically uncouple the cytoskeletal meshworks of cells from the junctions and disrupt the

212   formation of supracellular structures in the mesoderm (Figure 4 A, Supplemental Movies S1,

213   2) (Fernandez-Gonzalez and Zallen, 2011; Martin et al., 2010; Yevick et al., 2019). In α-

214   catenin-RNAi embryos, ventral cell apical area remains at pre-gastrulation levels (about 40

215   μm^2), but myosin contracts into spot-like structures at the apical cell surface (Figure 4 A , B,

216   E) (Martin et al., 2010). Quantification showed that, despite the lack of mechanical coupling,

217   active myosin reproducibly accumulated in a gradient around the ventral midline (Figure 4 C,

218   E). Therefore, graded myosin activation across the tissue does not depend on force

219   transmission between cells. However, the shape of the gradient appeared less sigmoidal in

220   α-catenin-RNAi, suggesting that mechanical feedback could affect gradient shape.

221   We then asked whether mesodermal F-actin depletion depends on intact adherens

222   junctions. Adherens junctions are a known target of Snail in the mesoderm (Chanet and

223   Schweisguth, 2012; Dawes-Hoang et al., 2005; Kolsch et al., 2007) and adherens junction

224   components exhibit a similar tissue-level pattern to F-actin (Supplement to Figure 4A). We

225   examined F-actin by staining α-catenin-RNAi embryos with phalloidin. Similar to wild-type

226   embryos, F-actin in α-catenin-RNAi embryos was depleted across the mesoderm with a

227 sharp boundary to the ectoderm before the start of contractile behavior (Figure 4 D, E). This

228 suggested that F-actin regulation by Snail does not depend on intact junctions. Depletion in

229 lateral mesoderm cells was maintained over time despite a lack of stretching in those cells.

230 Interestingly, junctional F-actin levels around the midline did not appear to be increased the

231 same as in wild-type embryos during constriction. However, medio-apical F-actin foci

232 appeared, which co-localized with myosin, presumably because actomyosin was uncoupled

233 from intercellular junctions (Supplement to Figure 4 B). These results indicated that F-actin

234 depletion in the mesoderm does not require intact adherens junctions and is not caused by

235 cell stretching.

236

237 **RhoA activation level modulates actomyosin gradient width within F-actin depleted**

238 **zone**

239 The above results suggested a Twist activity gradient leads to a RhoA activation gradient.

240 However, the gradient in Twist mRNA and accumulated T48 transcripts extends beyond the

241 5-6 cell rows from the ventral midline where we detect RhoA activation (Heer et al., 2017;

242 Lim et al., 2017; Rahimi et al., 2019). Therefore, we hypothesized that the gradient in Twist

243 activity is not simply transmitted, but is shaped by the signaling network downstream of

244 Twist. Mesodermal RhoA signaling involves a signaling circuit, which includes an

245 activator/inhibitor pair (Figure 3A). The activator RhoGEF2 is required for high levels of

246 apical myosin accumulation (Dawes-Hoang et al., 2005; Nikolaidou and Barrett, 2004). The

247 inhibitor, C-GAP, has been shown to disrupt proper subcellular myosin localization when

248 severely depleted in ventral cells (Mason et al., 2016). To test the importance of this circuit in

249 regulating the coordination of contractility, we quantified actomyosin contractility in embryos

250 where either C-GAP or RhoGEF2 levels were tuned to an extent that did not fully disrupt

251 subcellular myosin localization, but did change tissue-wide patterning.

252   First, we examined apical, activated myosin after elevating net RhoA activation by

253   either depleting C-GAP by RNAi (C-GAP-RNAi) or overexpressing RhoGEF2 (RhoGEF2

254   O/E). These perturbations elevated myosin in mesoderm cells, but did not elevate

255   contractility in the ectoderm at this stage (Figure 5 A). C-GAP-RNAi does not prevent basal

256   myosin loss in mesoderm cells (Mason et al., 2016), suggesting that this perturbation

257   specifically affects contractility on the apical side. In control embryos, apical myosin is

258   activated within 5 cells from the ventral midline. In contrast, C-GAP-RNAi and RhoGEF2 O/E

259   extended myosin activation to 7-8 cells away from the midline, with 3-4 cells on each side of

260   the ventral midline having uniformly high myosin intensity (Figure 5 B). C-GAP-RNAi also

261   extended the width of RhoA activation as detected by the active RhoA sensor (Supplement

262   to Figure 5 A). Consistent with the expansion of contractility, measurements of apical area

263   demonstrated that C-GAP-RNAi and RhoGEF2 O/E resulted in a wider zone of uniform

264   apical constriction, which changed from 2 cells on either side of midline up to 4 cells on each

265   side (Figure 5 C). Thus, our data suggested that increasing RhoA activation through C-GAP

266   depletion or RhoGEF2 overexpression widens the activated myosin gradient.

267   Next, we examined how increasing RhoA activation affected the F-actin pattern. We

268   found that, similar to its effect on myosin, increased net RhoA activation expanded the zone

269   of higher F-actin levels around the ventral midline, which is consistent with RhoA regulating

270   actin (Fox and Peifer, 2007). The increased width of F-actin elevation resulted in a narrower

271   region of depleted F-actin (Figure 5 D) without changing the position of the mesoderm-

272   ectoderm boundary (Supplement to Figure 5 B). In some cases, RhoGEF2 O/E completely

273   eliminated the pattern of F-actin depletion and elevation across the mesoderm during folding

274   (Figure 5 D), presumably because ventral F-actin accumulation expanded to the whole

275   mesoderm. In contrast, RhoGEF2 depletion resulted in a wider region of depleted F-actin

276   (Figure 5 E). Of note, RhoGEF2 depletion decreased the density of myosin-accumulating

277   cells and overall myosin levels, but did not visibly narrow the myosin gradient (Supplement

278   to Figure 5 C), suggesting that F-actin and myosin induction might be differently sensitive to

279 RhoA levels in our experimental setup. By quantifying the number of cell rows with depleted

280 F-actin, we found that the width of F-actin depletion appears inversely related to net RhoA

281 activation (Figure 5 F). Thus, the level of RhoA activation set by the GEF/GAP balance

282 determines the width of the F-actin gradient within the larger zone of F-actin depletion.

283

Myosin pulses elicit different area responses in midline versus margin mesoderm cells

286 So far, we focused on the patterns of average intensity and area in cell rows at a single

287 timepoint; however, myosin contractility in the ventral furrow is highly dynamic and exhibits

288 pulses (Martin et al., 2009). Myosin pulses are discrete events in which there is a burst of

289 myosin accumulation and often constriction of the cell apex. RhoA activity levels determine

290 the contractile outcome of a myosin pulse in individual cells (Mason et al., 2016). Given that

291 RhoA activity is graded across the furrow (Figure 3), we examined the behavior of myosin

292 pulses throughout the mesoderm. There are distinct classes of myosin pulses that are

293 known to occur in constricting cells during furrow formation. 'Ratcheted pulses' are events

294 where apical, active myosin persists after a pulse and decreased apical area is sustained

295 (Figure 6 A). In contrast, 'unratcheted pulses' exhibit myosin dissipation after the pulse and

296 exhibit cell relaxation. There is a continuum of behaviors from ratcheted to unratcheted,

297 which are associated with high and low RhoA activity, respectively (Mason et al., 2016).

298 Myosin pulse behavior in stretching cells is not well understood.

299   To determine whether the ventral-lateral gradient in RhoA patterns myosin pulse

300 type, we examined myosin persistence across different cell rows. Consistent with previous

301 measurements of contractile pulses in the middle of the ventral furrow (Xie and Martin,

302 2015), pulses close to the ventral midline exhibited persistent myosin; the myosin level after

303 the pulse was higher than the baseline before the pulse (Figure 6 B, cell row 1). Myosin

304 persistence was associated with a sustained decrease in apical area (Figure 6 C, cell row 1)

305   (Xie and Martin, 2015). In contrast, myosin pulses in more lateral mesoderm cells (Figure

306   6C, cell row 4) did not exhibit strong myosin persistence (Figure 6 B, cell row 7). These

307   myosin pulses were associated with area constriction, but cells partially relaxed after each

308   pulse. In marginal mesoderm cells (Figure 6C, cell row 7), myosin pulses still occurred, but

309   exhibited even less persistence. These myosin pulses accompanied cell stretching and did

310   not robustly result in cell apex constriction (Figure 6 C, cell row 7). Comparing pulse

311   behavior across different ventral-lateral positions, we found a graded decrease in myosin

312   persistence and area stabilization after pulses with distance from the ventral midline (Figure

313   6D), with marginal cells increasing their area during myosin pulses.

314   To confirm the differences in myosin pulses that we observed by determining the

315   average pulse behavior, we examined the cross-correlation between the constriction rate

316   (positive for apical area decrease) and the rate of myosin density change in cells along the

317   ventral-lateral axis, independently of pulse detection. Consistent with cell apical constriction

318   occurring during a myosin pulse, cells closest to the ventral midline exhibited a strong

319   positive correlation (Figure 6 E). Peak correlation decreased gradually up to 5 cells from the

320   ventral midline (Figure 6 E). Cells ~7-8 rows from the midline, in which apical area increases

321   during a myosin pulse (Figure 6 C), exhibited a negative correlation, indicating that these

322   cells with lower F-actin levels (Figure 1) stretch specifically when myosin increases (Figure 6

323   F). This behavior was specific to mesoderm cells at this stage because ectoderm cells did

324   not exhibit either a positive or negative correlation (Figure 6 G, cell rows 11, 12). Thus, there

325   are different myosin pulse behaviors depending on ventral-lateral position in the mesoderm.

326

327   The actomyosin gradient width regulates furrow curvature and lumen size

328   To examine the role of the wild-type contractile pattern in ventral furrow formation, we tested

329   how disrupting this pattern affected tissue shape. In wild-type embryos with graded

330   constriction, the ventral furrow is a sharp, v-shaped fold with high curvature at its center

331   (Figure 7A). Previous work showed that globally changing cell fate to create a much wider

332   mesoderm and contractile domain lowered the curvature of the furrow (Heer et al., 2017).

333   However, these experiments disrupted cell fate across the entire embryo. Here, we

334   investigated the role of the actomyosin gradient in folding, independently of cell fate. Upon

335   identifying C-GAP, we had found that some C-GAP-RNAi embryos have a more C-shaped,

336   less sharp fold (Mason et al., 2016). Therefore, we directly tested how widening the gradient

337   with C-GAP-RNAi or RhoGEF2 O/E affected the curvature of the ventral furrow. C-GAP-

338   RNAi and RhoGEF2 O/E embryos with a wider myosin gradient often had lower central

339   curvature than in wild-type (Figure 7 B and C, Supplement to Figure 7A and B). However,

340   the RhoGEF2 O/E phenotype was variable and the mean curvature was not significantly

341   different from control embryos (Figure 7 B and C, Supplement to Figure 7A and B). Most

342   embryos with low central curvature still fold successfully, although in some extreme cases

343   the mesoderm was not internalized. Successful folding in C-GAP-RNAi and RhoGEF2 O/E

344   embryos was associated with a significantly enlarged lumen when invaginated mesoderm

345   formed a tube (Fig. 7C).

346   Conversely, decreased RhoA activation in RhoGEF2-RNAi caused higher central

347   curvature (Supplement to Figure 7A, B). Although these embryos appeared to fold

348   successfully, in some cases, cells at the embryo surface, around the ventral midline,

349   underwent cell division immediately after invagination (Supplemental Movies S3,4). Because

350   the mesoderm is mitotic domain 10 (Foe, 1989), this suggests that a narrower band of

351   mesoderm invaginated and that some marginal mesoderm cells were left outside.

352   To explore the relationship between the contractile pattern and fold curvature further,

353   we tested whether the contractile pattern of an individual embryo is correlated with tissue

354   curvature in that embryo at a later time during folding. We segmented and binned cells from

355   12 live-imaged embryos (4 per genotype) to obtain their tissue-wide myosin and constriction

356   patterns. The same embryos were subsequently followed to measure cross-sectional tissue

357   curvature (averaged across three points along the anterior-posterior axis) at about 10 µm

358   invagination depth during folding and lumen size after folding. Linear regression analysis

359   revealed that the half-maximal gradient width was inversely correlated with curvature (Figure

360   7D). Consistent with the actomyosin gradient width determining the number of F-actin

361   depleted cell rows, the number of F-actin depleted cell rows was also correlated with

362   curvature in a separate experiment (Supplement to Figure 7C). Thus, gradient width and the

363   number of F-actin depleted cell rows are defining factors of the curvature of the ventral

364   furrow.

365 **Discussion**

366 Here, we showed that tissue folding is coordinated by cell shape changes across the tissue

367 that emerge from the combination of overlapping transcription factor and signaling patterns

368 (Figure 7 E). First, we found that there is a Snail-mediated uniform decrease in cortical F-

369 actin levels across the mesoderm. This decrease persists in cells at the lateral margin of the

370 mesoderm, with a sharp boundary to higher F-actin-containing ectoderm cells. Second, we

371 found that Twist activity that is refined by RhoA regulation gives rise to a gradient of

372 actomyosin. We showed that RhoA activation occurs in a tissue-level gradient and that

373 modulating the balance of RhoGEF2 to C-GAP shifts the width of this gradient. Importantly,

374 the levels and dynamics of myosin and F-actin in distinct cell groups are correlated with their

375 shape changes, leading us to speculate that differences in F-actin density and myosin

376 persistence between cell groups determine apical constriction vs. stretching behavior across

377 the ventral domain (Figure 7 E).

378 **Snail-mediated uniform mesodermal F-actin depletion**

379 We observed that during folding, cells with high F-actin levels tend to maintain their shape or

380 constrict, whereas low-F-actin cells stretch. The role of F-actin cortex density in a cell's

381 response to mechanical stress is well documented (Stricker et al., 2010). In the marginal

382 mesoderm, lower cortical F-actin levels in stretching cells is compounded by lower levels of

383 zonula adherens proteins (Dawes-Hoang et al., 2005; Kolsch et al., 2007; Weng and

384 Wieschaus, 2016), both of which could promote the ability of these cells to remodel and

385 stretch in response to stress. In contrast, the neighboring ectoderm and the medial ventral

386 cells have high F-actin and adherens junction density, which may help those cells maintain

387 their shape or even constrict under stress. Importantly, the effect of Snail on F-actin is

388 independent of functional adherens junction assembly, suggesting that Snail targets several

389 cellular processes in parallel to promote mesoderm cell remodeling.

390   Alternatively, it was possible that cell strain/stretching or constriction contributed to

391   decreased F-actin density (Latorre et al., 2018). However, the fact that F-actin depletion

392   occurs before stretching and is not disrupted when cells are prevented from constricting and

393   stretching their neighbors suggests that F-actin depletion is not driven by cell shape change.

394   In fact, the transcription factor Snail appears to uniformly deplete F-actin prior to cell shape

395   change. The mechanism by which Snail decreases F-actin is unknown and will be an area of

396   future study. Snail could possibly regulate F-actin assembly via Diaphanous or Enabled (Fox

397   and Peifer, 2007; Homem and Peifer, 2008), or F-actin disassembly via regulation of Cofilin

398   (Jodoin et al., 2015).

399   Twist and RhoA signaling create an actomyosin gradient within the Snail domain

400   Nested within this zone of Snail mediated F-actin depletion, Twist activity causes

401   actomyosin accumulation via graded RhoA activation. This combination of two overlapping

402   transcription patterns allows for domains of different cell behaviors and mechanical

403   properties within a tissue of uniform cell fate (mesoderm). We further found that patterning of

404   constricting and stretching domains is tightly regulated by the RhoA regulators RhoGEF2

405   and C-GAP; disrupting that pattern even slightly causes changes to the shape of the

406   resulting fold. RhoGTPases are regulated by complex interactions between their (activating)

407   GEFs and (inhibiting) GAPs in many contexts (Denk-Lobnig and Martin, 2019); in the ventral

408   furrow specifically, interactions between C-GAP and RhoGEF2 tune sub-cellular localization

409   and dynamics of the contractile apparatus during folding (Mason et al., 2016). Here, we

410   found that small changes to C-GAP or RhoGEF2 levels, which do not strongly disrupt cell-

411   level organization, change the pattern of actomyosin levels across the ventral domain.

412   Specifically, this property is dependent on the ratio of RhoGEF2 and C-GAP, or net RhoA

413   activation: C-GAP RNAi and RhoGEF2 O/E both widen the domain of high actomyosin, and

414   create a uniform high-contractility domain around the ventral midline. Conversely, RhoGEF2

415   RNAi narrows the F-actin gradient and furrow, and creates a wider domain of F-actin-

416   depleted cells.

417   Our data suggests a system with a graded activator (RhoGEF2) and a uniform

418   inhibitor (C-GAP), in which the inhibitor buffers overall activation and creates an activation

419   threshold (Figure 7 E). We propose that the activation threshold regulates the width of the

420   actomyosin gradient: the gradient widens if overall activator levels increase or inhibitor levels

421   decrease; it narrows if the activator level is decreased. A widened central region of uniform

422   contractility can emerge if some part of the system is saturated at sufficient RhoA activation

423   levels, consistent with our measurements of the contractile gradient in RhoGEF2 O/E and C-

424   GAP-RNAi embryos. If RhoA activation is decreased, such as in RhoGEF2 RNAi embryos,

425   this mechanistic model predicts a narrower gradient. This appears to be true for the F-actin

426   pattern.

427   Myosin levels in RhoGEF2-RNAi were decreased overall and fewer cells

428   accumulated myosin, but the myosin gradient width was the same as in wild-type. F-actin

429   and myosin may respond to low RhoA activity because they have different thresholds for

430   accumulation, possibly because they are controlled by different regulators downstream of

431   RhoA or. In addition, expression of fluorescently tagged Utrophin actin-binding domain,

432   which disrupts F-actin dynamics (Spracklen et al., 2014), appears to interact with RhoA

433   disruptions, amplifying the phenotype of high RhoA activation and reducing the cell-level

434   effects of RhoGEF2 RNAi. This is consistent with the notion that RhoA activation promotes

435   F-actin assembly across the tissue.

436   A prediction of this model is that the upstream activator RhoGEF2 should be graded

437   over a wider region in wild-type than the downstream myosin. Our measurements of

438   RhoGEF2::GFP show a gradient of similar width as myosin, however the small signal-to-

439   noise ratio of the RhoGEF2::GFP probe could obscure the lateral tails of that gradient. The

440   upstream *twist* mRNA and T48 protein gradient is several cells wider than the myosin

441   gradient (Heer et al., 2017), consistent with a possibly wider activation gradient of RhoGEF2.

442   Our data show that the gradient shape is tuned by a RhoA activator-inhibitor pair.

443   There are other points in the pathway where balance between inhibition and activation is

444   likely to contribute to tissue-wide patterning. In particular, GPRK2, an inhibitor of GPCR

445   signaling, affects myosin organization and cell behaviors (Fuse et al., 2013; Jha et al., 2018).

446   In GPRK2 mutant embryos, apical constriction is expanded, such that lateral mesoderm cells

447   that normally stretch accumulate myosin and constrict (Fuse et al., 2013). This is consistent

448   with a potential role for GPRK2 restricting the contractile gradient. Further downstream,

449   myosin activity is regulated directly by the balance of ROCK and myosin phosphatase

450   (Munjal et al., 2015; Vasquez et al., 2014) and several actin regulators tune the balance of

451   F-actin assembly and disassembly in ventral furrow formation (Fox and Peifer, 2007;

452   Homem and Peifer, 2008; Jodoin et al., 2015). Control of tissue-wide properties by

453   overlapping patterns of regulators, such as F-actin regulation by Snail and Twist and

454   actomyosin gradient regulation by C-GAP and RhoGEF2, appears to be a powerful

455   mechanism to create complex spatial patterns of cell behavior.

456   **Fold curvature is tuned by tissue-wide actomyosin patterning**

457   Our disruptions of the actomyosin gradient demonstrate that tissue curvature is

458   sensitive to tissue-wide contractile patterns. The width and position of the contractile

459   gradient is important for the shape of the resulting fold. We showed that adjusting the width

460   of actomyosin gradient by modulating the levels of RhoGEF2 or C-GAP influences tissue

461   curvature. Elevating RhoA activity creates a wider gradient and results in C-shaped furrows

462   with low curvature. By using inherent patterning variability in wild-type and extended

463   variability in genetic disruptions, we showed that the contractile pattern of an individual

464   embryo is correlated with subsequent folding and post-fold shape, suggesting that it would

465   be possible to partially predict tissue curvature based on the observed myosin pattern of an

466   embryo. This is consistent with past work suggesting that broadening contractility lowers

467   tissue curvature. For example, depletion of the ventral fate inhibitor, Serpin27A, caused a

468   wider mesoderm, to form an abnormally shallow furrow (Heer et al., 2017). Similarly, in

469   GPRK2 mutants, which do not affect the width of the mesoderm, all cells within the

470   mesoderm (~18 cells) constrict and create a U-shaped furrow that often fails to close (Fuse

471   et al., 2013). How F-actin patterning is affected in either of those cases is not known.

472   That increased contractility in the tissue decreases fold curvature may seem counter-

473   intuitive, but computational modeling shows that graded contractility creates a sharper fold

474   than uniformly high contractility (Heer et al. 2017). Force balance between neighboring high-

475   contractility cells prevents efficient constriction in the uniform case, whereas in the graded

476   case, central high-contractility cells can constrict efficiently against their lower-contractility

477   neighbors, causing a sharp hinge. Considering that successful constriction of cells is

478   dependent on the mechanics of their neighbors, it is plausible that the stretching lateral

479   mesoderm domain can further promote higher curvature folds (Ko et al., 2020; Perez-

480   Mockus et al., 2017; Sui et al., 2018). While we were not able to specifically change F-actin

481   levels because of pleiotropic effects of modulating F-actin dynamics (Jodoin et al., 2015), we

482   speculate that changes to the width of the "soft", F-actin depleted domain, concomitant with

483   changing gradient width, likely contributed to our observed folding phenotypes. Ventral

484   furrow formation is an embryo-wide mechanical process: it depends on embryo shape

485   (Chanet et al., 2017) and relates to cell shape changes on the opposite, dorsal side of the

486   embryo (Rauzi et al., 2015). Our results further emphasize the importance of understanding

487   tissue-wide mechanics during folding.

488   Development generates a multitude of tissue curvatures in different contexts. We

489   showed that folding is sensitive to small patterning changes of actomyosin. Our discovery

490   suggests a mechanism by which actomyosin and mechanical cell properties might be

491   patterned in other tissues to generate distinct curvatures.

492

Materials and Methods

Fly stocks and crosses

For a list of fly stocks and crosses used in this study, see Supplemental Table S1.

An N-terminal GFP tag was inserted at the endogenous C-GAP locus using CRISPR-Cas9 as previously described (Gratz et al., 2015). Coding sequences for two 15 base pair (bp) gRNAs targeting neighboring sites 5' of the *rhoGAP71E* gene start codon were cloned into the pU6-BbsI plasmid using the CRISPR Optimal Target Finder (Gratz et al., 2014; Iseli et al., 2007). The donor template plasmid for homology directed repair was generated using Exponential Megapriming PCR (Ulrich et al., 2012). A plasmid backbone (from pHD scarless DS Red) containing an ampicillin resistance gene and an origin of replication was combined with two homology arms (1219 bp and 1119bp, respectively) homologous to the region around the *rhoGAP71E* gene start codon, flanking a *GFP* encoding DNA sequence (kindly provided by Iain Cheeseman) with an N-terminal 4 amino acid-encoding linker region (Ser-Gly-Gly-Ser). Both plasmids were injected into nanos>Cas9 expressing embryos. Surviving adults were crossed to y,w; +;+ flies and then screened for mosaic GFP insertion by PCR. Progeny of GFP-positive injected flies were crossed to y,w;+;Dr/TM3 flies and then screened by PCR for the GFP insertion. Successful insertions were further analyzed by sequencing. The fly stock established from their offspring was later back-crossed once to OreR flies in order to eliminate potential off-target mutations. Homozygous C-GAP-GFP flies were viable, suggesting that the GFP-tagged C-GAP is functional.

Live and fixed imaging

Embryos were prepared for live imaging as previously described (Martin et al., 2009). Embryos were collected in plastic cups covered with apple-juice plates. Flies were allowed to lay eggs for 2–4 h at 25 °C (or temperature as noted in Table S1). The plate was removed and the embryos immersed in Halocarbon 27 oil for staging. Embryos undergoing

518   cellularization were collected. Embryos were dechorionated with 50% bleach, washed with

519   water, and then mounted on a slide with embryo glue (Scotch tape resuspended in heptane),

520   with the ventral side facing upwards. A chamber was made with two no. 1.5 coverslips as

521   spacers and was filled with Halocarbon 27 oil for imaging. Images were acquired on a Zeiss

522   710 microscope with an Apochromat 40×/1.2 numerical aperture W Korr M27 objective.

523   Channels were excited and detected concurrently.

524   Immuno- and phalloidin staining was performed using standard methods (Martin et

525   al., 2009). Embryos were fixed with 8% paraformaldehyde in PO_4 buffer and heptane (3:4)

526   for 30 min, devitellinized manually, stained with phalloidin, primary antibodies and

527   appropriate fluorescently tagged secondary antibodies, and mounted in AquaPolymount

528   (Polysciences, Inc.). Anti-snail (rabbit, 1:100; formaldehyde-hand peeled fixation; gift from M.

529   Biggin), anti-armadillo (mouse, 1:500; heat-methanol fixation; DSHB), anti-GFP (rabbit,

530   1:500; formaldehyde-hand peeled fixation; Abcam, ab290) and anti-E-cadherin (rat, 1:50;

531   formaldehyde-hand peeled fixation; DHSB) antibodies and AlexaFluor568 phalloidin

532   (Invitrogen) were used. All imaging was carried out on a Zeiss 710 confocal microscope with

533   a Plan-Apochromat 40×/1.2 numerical aperture W Korr M27 objective. Channels were

534   excited and detected concurrently.

535   For imaging settings for each fluorescent marker, refer to Supplemental table S2.

536

537   **Gradient analysis**

538   Analysis was done as described in Heer et al., 2017. All image analysis was performed

539   in Fiji (http://fiji.sc) (Schindelin et al., 2012) and MATLAB (MathWorks). Custom software for

540   image processing is available upon request.

541

542   **1) Definition of developmental timing**

543   Wild-type embryos were staged based on time of folding. The accuracy of this method

544   was confirmed by comparing constricted areas per bin at the selected time point. For

545   embryos with disrupted constriction and folding, a time point was chosen relative to the

546   beginning of myosin/ fluorescence accumulation.

547

548   **2) Shell projection and thresholding to measure apical fluorescence intensity**

549   Shell projections of the apical surface were conducted as previously described (Heer et

550   al., 2017). First, cytoplasmic background signal (defined as the mean cytoplasmic signal plus

551   2.5 standard deviations) was subtracted from the myosin channel (Martin et al., 2009;

552   Vasquez et al., 2014). For non-myosin fluorescent signal (Figure 3), the cytoplasmic

553   background subtraction was adjusted to account for differences in signal-to-noise ratio for

554   different fluorescent markers (RhoGEF2::GFP: mean + 2 standard deviations (SDs);

555   aniRBD::GFP: mean + 2 SDs , rok::GFP: mean + 2.5 to 3 SDs, GFP::C-GAP: no background

556   subtraction).

557   The maximum myosin (or other apically enriched fluorescent) signal intensity in the z-

558   plane was used to generate a rough map of the embryo surface. A Fourier transform was

559   used to generate a smooth continuous surface. Myosin signal was averaged over the 4 μm

560   above the surface and membrane signal was the sum of the signal from 1-2 μm below the

561   surface. A gaussian blur filter (radius 1 pixel for fluorescent signal, 0.7-1 membranes) was

562   applied after shell projection to reduce noise.

563   Shell projections from live and immunostained images were then segmented using

564   an existing MATLAB package, Embryo Development Geometry Explorer (EDGE) (Gelbart et

565   al., 2012). Membrane signal (Gap43::mCherry) or cortical F-actin (phalloidin or Utr::GFP)

566   projections were used to detect cell boundaries (and track cells for live images). Myosin (or

567   equivalent signal) shell projection was used to measure apical signal accumulation.

568   Segmentation errors in were corrected manually. Our segmentation algorithm was used to

569   determine centroid position, cell diameter, cell area, cell perimeter as well as total

570   myosin/fluorescence signal per cell.

571

572   **3) Cell bins**

573   For all image quantification, data was segregated into 'cell bins' i.e. cell rows relative to the

574   ventral midline (Heer et al. 2017). Cells were assigned to bins based on the ventral-lateral

575   position of the cell centroid. The ventral midline was defined as the position at which the

576   furrow closes. In fixed images or for embryos that did not fold (or rotated while folding), the

577   position of the VM was determined by symmetry of the fluorescent signal and constriction.

578   Live images were binned based on initial position of the cell centroid before tissue

579   contraction and folding and the boundaries of the bins were set by the average cell diameter

580   along the ventral-lateral axis. For images in which cells had already begun to constrict, the

581   width of each bin was set manually (but still relative to average cell diameter) to approximate

582   the width of cells at that ventral-lateral position. We used MATLAB to generate box-and-

583   whiskers plots depicting the distribution of data, overlaid with the mean of each bin. For

584   boxplots, bottom and top sides of the box represent 25th and 75th percentile of cells,

585   respectively. Outliers were defined as values 1.5 times bigger than the interquartile range.

586   Fluorescent signal was normalized by dividing by the mean of the first bin to adjust for

587   variability in imaging conditions.

588   **Cortical F-actin quantification**

589   For apical projections of phalloidin staining (Figure 1A, 2A and 4B), embryos were

590   shell-projected and cells tracked the same way as for myosin and other markers (see

591   above), except that no background subtraction was applied. To measure cortical F-actin

592   intensity, we integrated the signal intensity of pixels within 2 μm of the identified cell

593   boundaries . This total junctional F-actin signal was divided by the cell perimeter to obtain

594   junctional F-actin density.

595   Because mesodermal F-actin depletion was most obvious subapically, not apically,

596   with Utrophin::GFP markers in live embryos (Figures 2B, 5C and 7C), those movies were

597   "shell-projected" in Fiji by generating a Z-reslice (1 µm per slice) and then creating a second

598   reslice along a manually drawn subapical line that followed the ventral-lateral curvature of

599   the embryo surface at about 10-15 µm below the apical surface (Supplement to Figure 2).

600   This allowed us to correct for specific ventral-lateral curvature and get a subapical projection

601   of constant z-depth from the embryo surface. The center part along the anterior-posterior

602   (AP) axis of the shell-projection, where AP curvature is small, was used to quantify F-actin

603   (Utrophin::mCH or ::GFP) intensity along the ventral-lateral axis. We used the FIJI "Plot

604   profile" command, averaging intensity across the AP length of the selection (consistent

605   between embryos) for each pixel row. Intensity profiles were exported, aligned based on

606   position of the ventral midline, smoothed with moving average smoothing (window-size 20)

607   and plotted in Matlab R2019a. Fluorescence signal was normalized by subtracting the mean

608   intensity, to adjust for variability in imaging conditions.

609   Cell rows depleted of F-actin (Figure 5D, Supplement to Figure 5C) were counted

610   manually on the subapicalprojections used for intensity profiles. If depleted regions on both

611   sides of an embryo were visible, both were counted and the average used. Differences in

612   depleted cell rows between genotypes were represented in a box plot using Matlab and

613   statistically compared using the non-parametric two sample Kolmogorov–Smirnov test.

614   **Pulsing analysis**

615   Images of live embryos with myosin and membrane markers during folding were

616   obtained as above, but with faster scan speed and smaller z-depth, to obtain time intervals

617   of 9 to 11 seconds between stacks, which is sufficient to capture typical myosin and area

618   pulsing behavior (Martin et al., 2009). Cells across the mesoderm were tracked over time

619   using EDGE, and cell area and myosin intensity were exported. Using Matlab 2019a, we

620   detected peaks within individual cells of maximal myosin intensity increase, smoothing with a

621   moving average filter and then detecting local maxima. The cell behavior about 100 seconds

622   before and after each maximum was saved as a trace. Pulse traces were averaged for each

623   cell bin to identify average dynamics based on cell position. Persistence of myosin pulses

624   was defined as the minimum myosin intensity within each trace after a peak minus minimum

625   myosin intensity before the same peak. Persistence of area constriction was defined as the

626   maximum cell area after a myosin peak minus maximum cell area before the same peak.

627   Each trace was normalized to the center of the pulse. Persistence values were averaged by

628   bin and plotted in Matlab for an individual embryo.

629   To analyze further the relationship between area and myosin behaviors, we cross-

630   correlated rates of myosin and area change (as described in Martin et al., 2009). We used

631   the xcorr function in Matlab to cross-correlate the change in myosin intensity (myosin

632   intensity at a timepoint minus myosin intensity at the previous time point) with constriction

633   change (cell area at a timepoint minus cell area at the next time point, i.e. cross- positive

634   value if constricting, negative if stretching) for each cell trace. Cross-correlations for each

635   cell were averaged by bin (distance from the midline) and plotted.

Curvature analysis

637   Movies of the embryos for which we had measured the multicellular myosin gradient

638   (see above) (with at least 20 μm z-depth) were resliced in FIJI to create 1 μm thick cross

639   section images of the ventral furrow at the middle of the AP axis of the embryo. Apically

640   enriched myosin signal was used to trace the surface of the folding tissue with the freehand

641   line tool in Fiji. The fold was traced for a cross section at the center of the AP axis of the

642   embryo as well as for cross-sections 20μm anterior and posterior, respectively. The

643   timepoint of measurement was chosen as when the invagination depth was ~ 10 μm. The

644   XY coordinates of each trace were imported into Matlab R2019a. After manually determining

645   the position of the ventral midline, a circle fit (Nikolai Chernov (2020). Circle Fit (Taubin

646   method)https://www.mathworks.com/matlabcentral/fileexchange/22678-circle-fit-taubin-

647   method), MATLAB Central File Exchange. Retrieved February 5, 2020) was applied to the

648   central part of the trace, 2.5 µm width around the midline. The inverse of the fitted circle

649   radius was defined as the fold curvature. The three traces taken at different AP positions

650   were averaged to obtain the fold curvature value for the embryo. Local curvature as

651   displayed in Figure 7 A and B was generated using LineCurvature2D (Dirk-Jan Kroon

652   (2020). 2D Line Curvature and

653   Normals (https://www.mathworks.com/matlabcentral/fileexchange/32696-2d-line-curvature-

654   and-normals), MATLAB Central File Exchange. Retrieved March 16, 2020.) in Matlab.

655   Post-fold lumen sizes were measured from central cross-sections of the same

656   embryos whose curvature had been analysed, for a single AP position. Lumen area was

657   measured by manually fitting an ellipse to the lumen in each cross-section in Fiji and

658   measuring its area.

659   Curvature and lumen measurements were compared between genotypes using the non-

660   parametric two sample Kolmogorov–Smirnov test.

661   **Regression analysis**

662   All linear regression fits (Figures 1C, 7D, S7C) were performed in Matlab R2019a

663   using the fitlm command. The original data as well as the best fit line were plotted and the R-

664   squared value and best fit slope were reported.

665   For myosin gradients, the position of the most lateral bin with myosin levels above

666   the half-maximal myosin intensity was used to define gradient width. This bin position was

667   then compared to central curvature measurements of the same embryo at a later timepoint

668   (at ~10 µm invagination depth, analyzed with circlefit). For Utrophin::GFP embryos, cell rows

669   with depleted F-actin were counted manually and compared to central curvature of the same

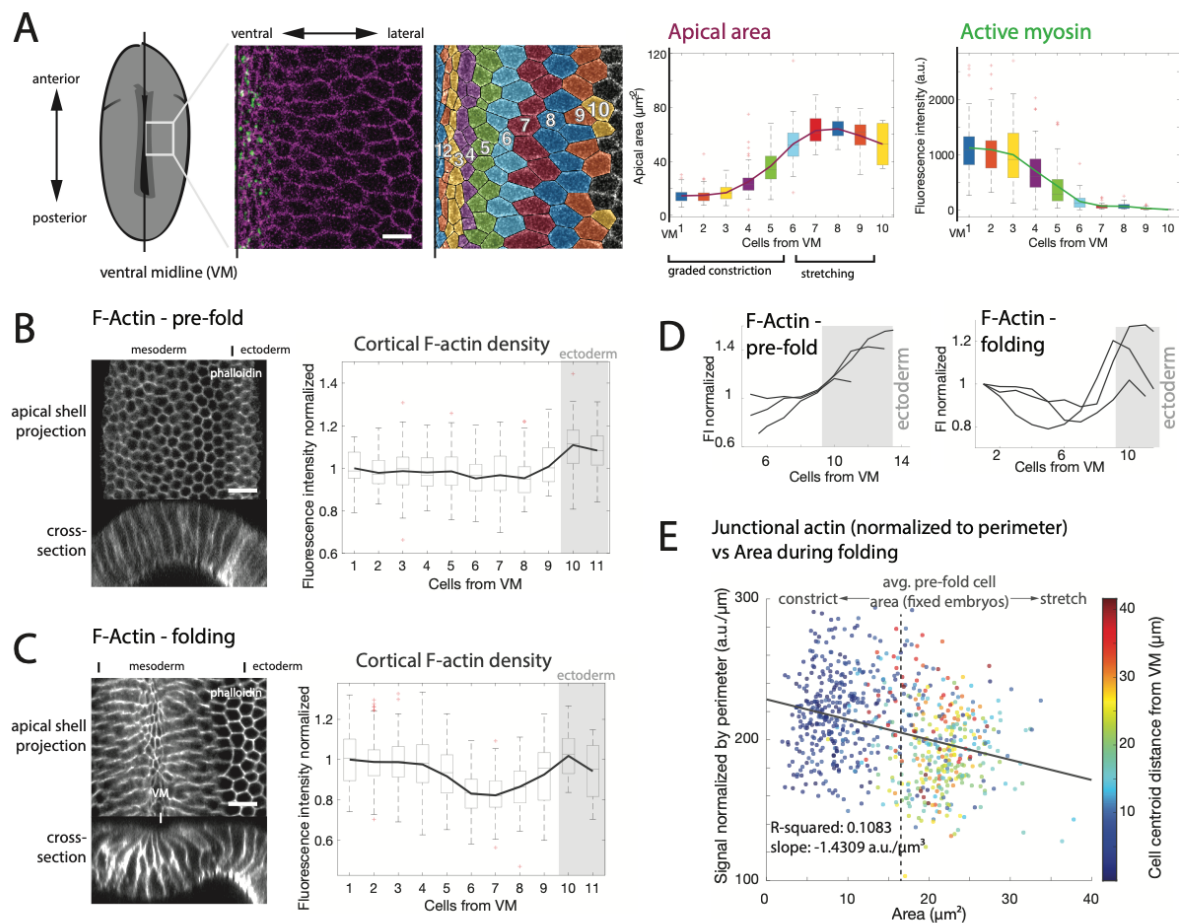670   embryo at a later timepoint (at ~10 µm invagination depth).

671

672

Acknowledgments

Figure legends

Figure 1. Tissue-wide mesodermal F-actin distribution is distinct from Myosin. (**A**) Myosin

gradient extends 6 cells from the ventral midline (VM) and remains low. Images are apical

surface view of embryo labeled with sqh::GFP (Myosin) and Gap43::mCherry (membrane)

and segmented example of embryo with cell rows highlighted in different colors. Scale bar =

10 µm. Colors in image correspond to bins in adjacent plots; showing Myosin and apical

area distributions in a representative wild-type embryo . Data is represented by box-and-

whisker plot, where bottom and top sides of the box represent 25th and 75th percentile of

cells, respectively. Midline is the median and red '+' are outliers. Box-and-whisker plot is

shown for one representative embryo (corresponds to image on left) with at least 4 cells per

bin analyzed (median 52.5 cells). (**B**) Left: F-actin is depleted at the mesoderm-ectoderm

695   border. Images are apical shell projection (top) or cross-section (bottom) images of

696   phalloidin stained embryos imaged before furrow formation. Scale bar = 10 μm. Right: Plot

697   showing F-actin depletion in the mesoderm. Mean cortical F-actin intensity was calculated

698   from segmented cells. Cortical F-actin density was calculated by integrating F-actin intensity

699   around the cell periphery and dividing by cell perimeter. Cortical F-actin density was

700   normalized to mean of first cell row. Data is represented by box-and-whisker plot, where

701   bottom and top sides of the box represent 25th and 75th percentile of cells, respectively.

702   Midline is the median and red '+' are outliers. Box-and-whisker plot is shown for one

703   representative embryo (corresponds to image on left) with at least 23 cells per bin analyzed

704   (median 52 cells). (**C**) Left: F-actin accumulates in a gradient across the ventral mesoderm.

705   Images are apical shell projection (top) or cross-section (bottom) images of phalloidin

706   stained embryos imaged during furrow formation. Scale bar = 10 μm. Right: Plot showing F-

707   actin depletion in the mesoderm. Mean cortical F-actin intensity was calculated and data

708   represented the same as (B). Box-and-whisker plot is shown for one representative embryo

709   (corresponds to image on left) with at least 15 cells per bin analyzed (median 73 cells). (**D**)

710   Mean F-actin density traces for 3 embryos corresponding to (B) (pre-fold F-actin) and (C) (F-

711   actin during folding), normalized by mean of 9th and 1st cell row, respectively. (**E**) Apical area

712   is inversely correlated with cortical F-actin levels. Quantification of cortical F-actin density

713   per cell (cortical F-actin intensity divided by perimeter) for the embryo shown in (C) was

714   plotted as a function of apical area. Color of data points represents physical distance from

715   ventral midline in μm. Average pre-fold cell area for fixed embryos (~16 $μm^2$ due to

716   shrinkage during the fixation process) is indicated with dotted grey line. Note that cells

717   towards the margin of the mesoderm have the largest area and lowest F-actin and cells

718   farther out (i.e., ectoderm) have an area centered at ~16 $μm^2$ and higher F-actin levels.

719
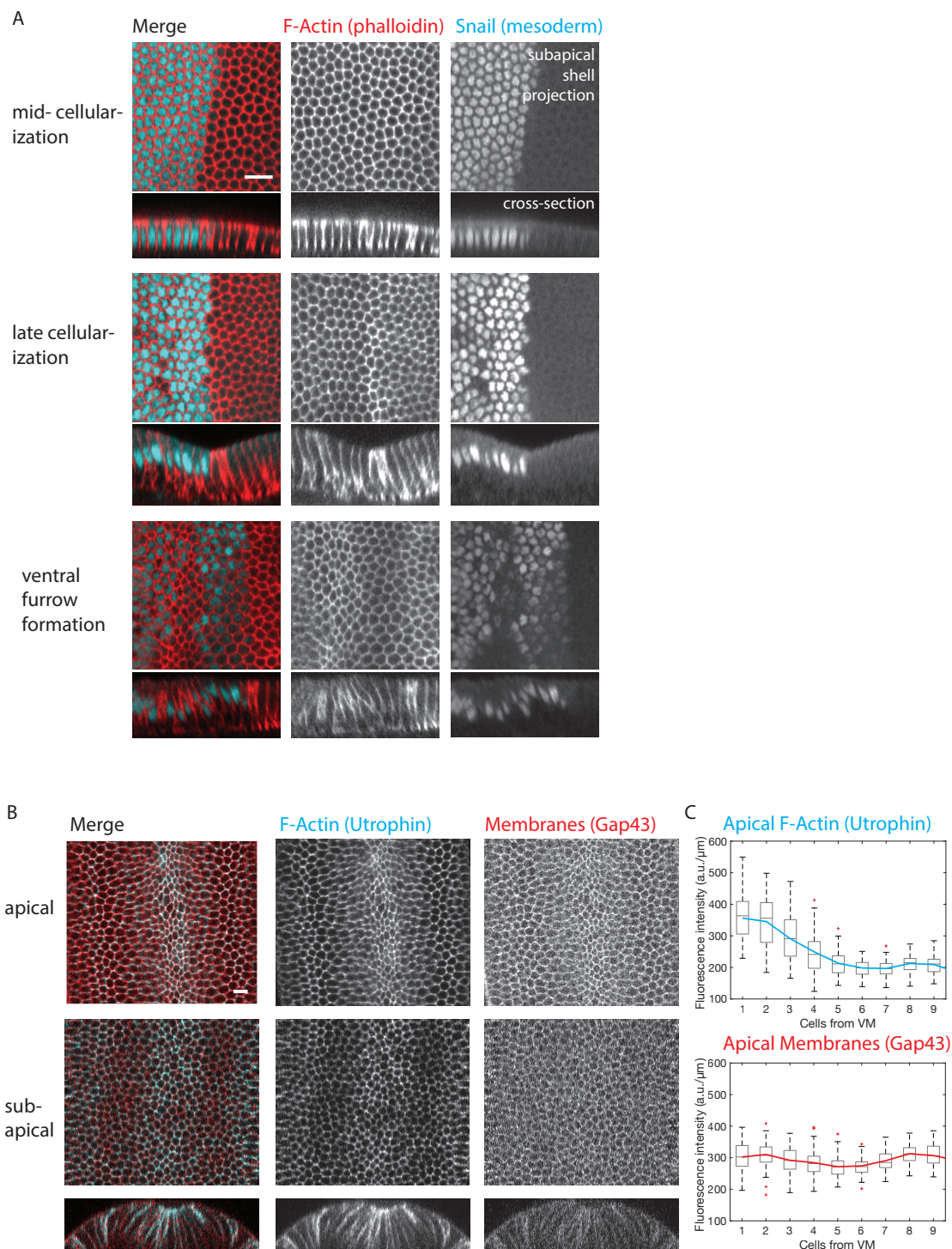
Supplement to Figure 1. F-actin is depleted in the mesoderm during cellularization. (**A**) F-actin depletion in the mesoderm is not present in early cellularization, but appears towards the end of cellularization. Images are subapical shell projections (top) and cross-sections (bottom) of wild-type embryos at different stages stained with phalloidin (red) and anti-snail antibody (cyan). Scale bar = 10 μm. Bending of tissue during late cellularization in cross-

725   section is a fixation artefact. (**B**) F-actin marked by the fluorescently marked Utrophin::GFP

726   (cyan) is depleted in the marginal mesoderm, but a general membrane marker,

727   Gap43::mCherry (red), is not. Images show both markers in apical (top) and subapical

728   (middle) shell projections and cross-sections. Scale bar = 10 μm. (**C**) Quantification by bin of

729   apical Utrophin::GFP (top) and Gap43::mCherry (bottom) junctional fluorescent intensity,

730   divided by perimeter. Although less pronounced, apical Utrophin::GFP shows a similar

731   pattern to phalloidin, with low F-actin density in lateral mesoderm cells compared to

732   ectoderm cells. Data is represented by box-and-whisker plots where each bin is a cell row at

733   a given distance from the ventral midline (at least 67 cells per row analyzed, median 72

734   cells). Bottom and top sides of the box represent 25th and 75th percentile junctional intensity

735   per cell, respectively. Midline is the median and red '+' are outliers.
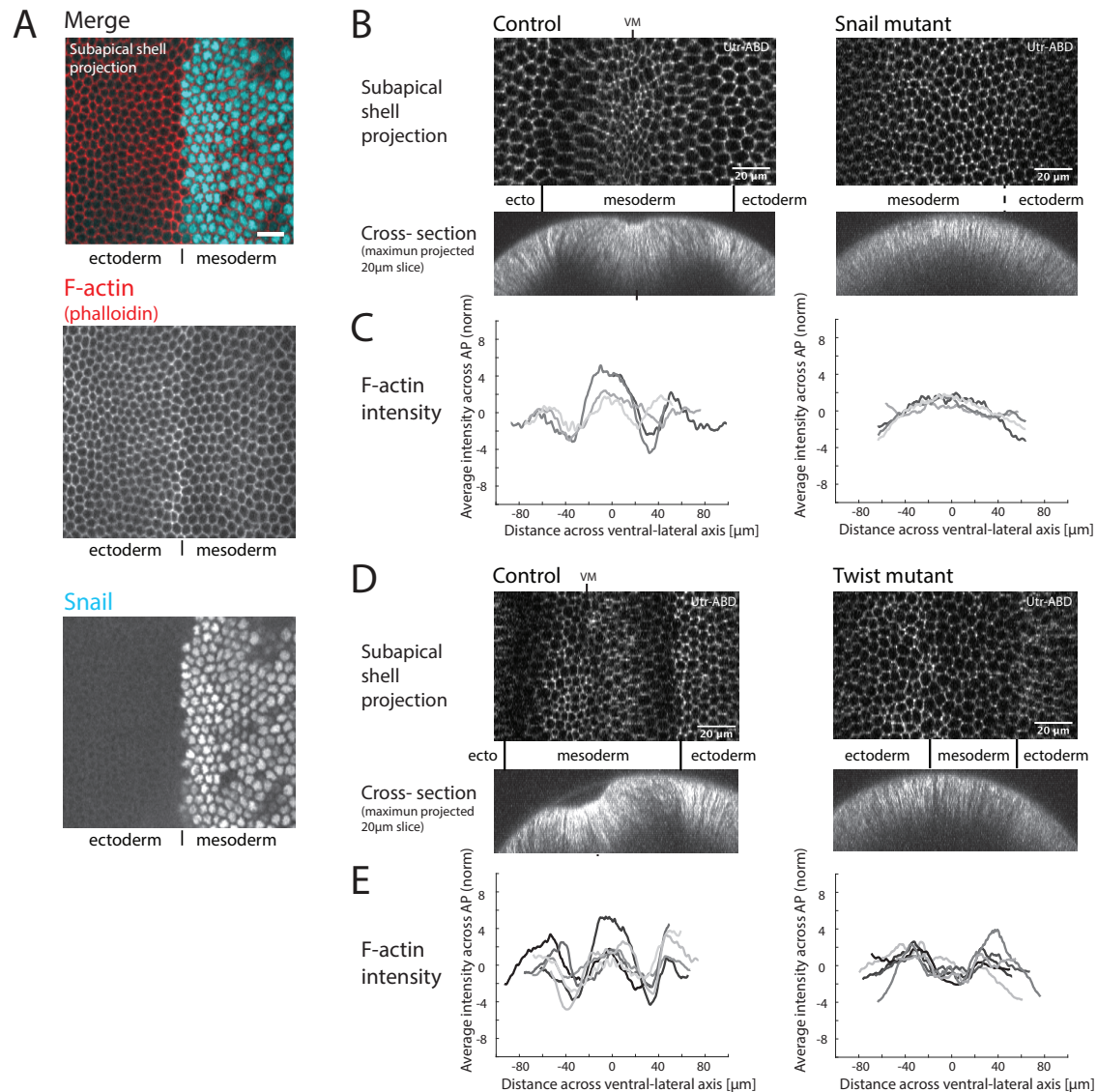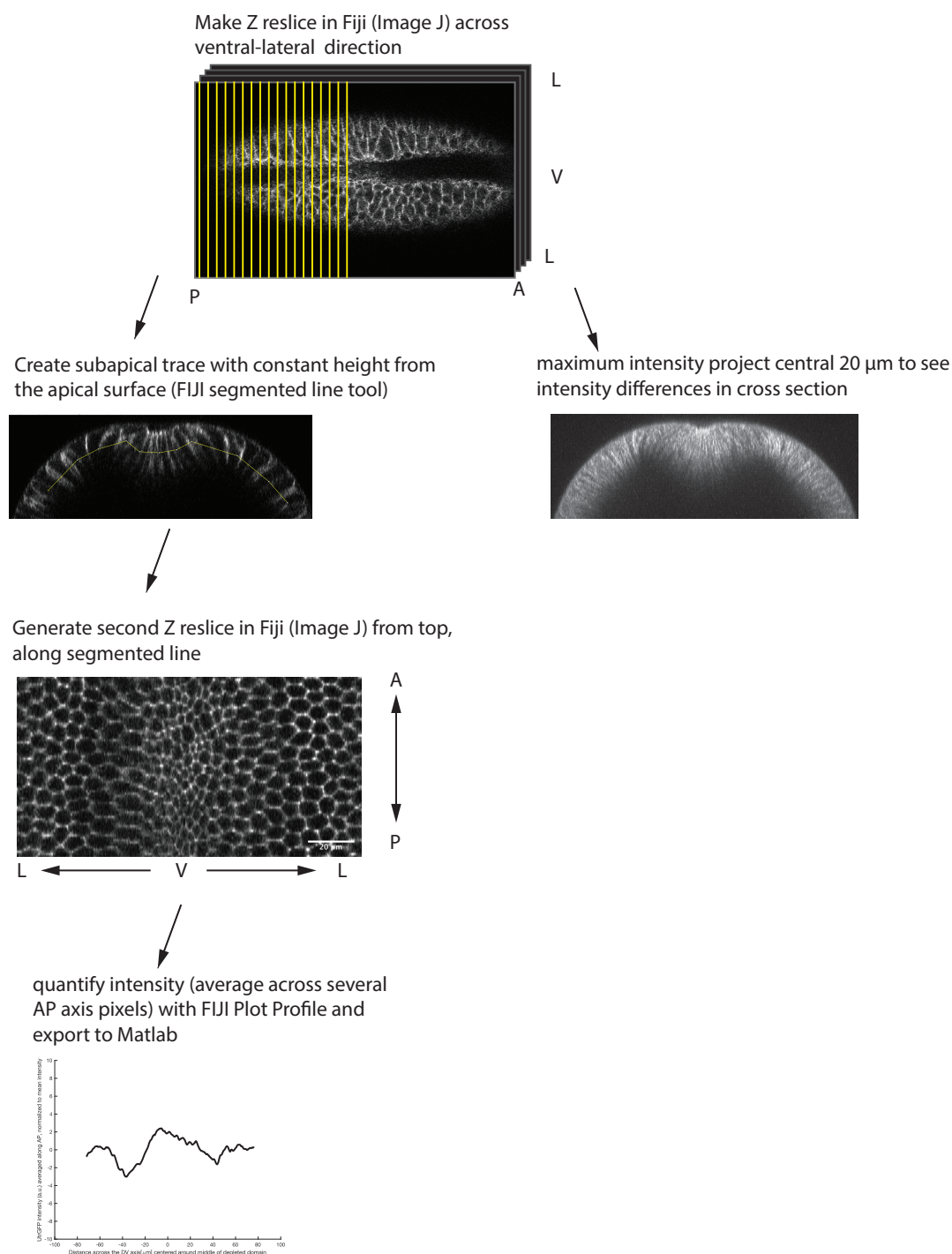
736

737

Figure 2. Snail and Twist distinctly regulate the tissue-wide F-actin distribution. (**A**) Snail expression boundary corresponds to F-actin depletion boundary. Images are from phalloidin-stained embryo co-stained with anti-Snail. Scale bar = 10 μm. (**B**) The *snail* mutant disrupts mesodermal F-actin depletion. Images are from representative, live homozygous *snail* mutant and normal sibling embryo expressing Utrophin::GFP (F-actin). The *snail* mutant shows a lack of F-actin patterning. Scale bar = 20 μm. (**C**) Quantification of tissue-wide F-actin intensity profiles from 4 *snail* mutant and 4 normal sibling embryos (See Methods and Supplement to Figure 2). All *snail* mutants lack F-actin patterning. The decreased F-actin intensity at the edges of the ventral-lateral axis reflects the curvature of the tissue, which

747   causes more tissue to scatter light between objective and more lateral parts of the projected

748   layers. (**D**) The *twist* mutant exhibits F-actin depletion, but lacks F-actin elevation around

749   midline. Images are from 6 representative, live homozygous *twist* mutant and 6 normal

750   sibling embryos expressing Utrophin::GFP (F-actin). The *twist* mutant exhibits F-actin

751   depletion. Scale bar = 20 μm. (**E**) Quantification of tissue-wide F-actin intensity profiles from

752   multiple *twist* mutant and normal sibling embryos. All *twist* mutants exhibit F-actin depletion,

753   but not the increase around the midline.

754

Workflow for subapical shell projections:

Make Z reslice in Fiji (Image J) across ventral-lateral direction

Create subapical trace with constant height from the apical surface (FIJI segmented line tool)

maximum intensity project central 20 µm to see intensity differences in cross section

Generate second Z reslice in Fiji (Image J) from top, along segmented line

quantify intensity (average across several AP axis pixels) with FIJI Plot Profile and export to Matlab

755

Supplement to Figure 2. Workflow for subapical shell projections in FIJI. Confocal image stacks are resliced along the ventral-lateral axis to get a cross-sectional view. A subapical trace is then drawn manually about 10-15 µm below the apical surface and the embryo is

759   resliced a second time along the trace. The central part of the embryo along the AP axis is

760   then used to quantify intensity along the ventral-lateral axis.

761

762
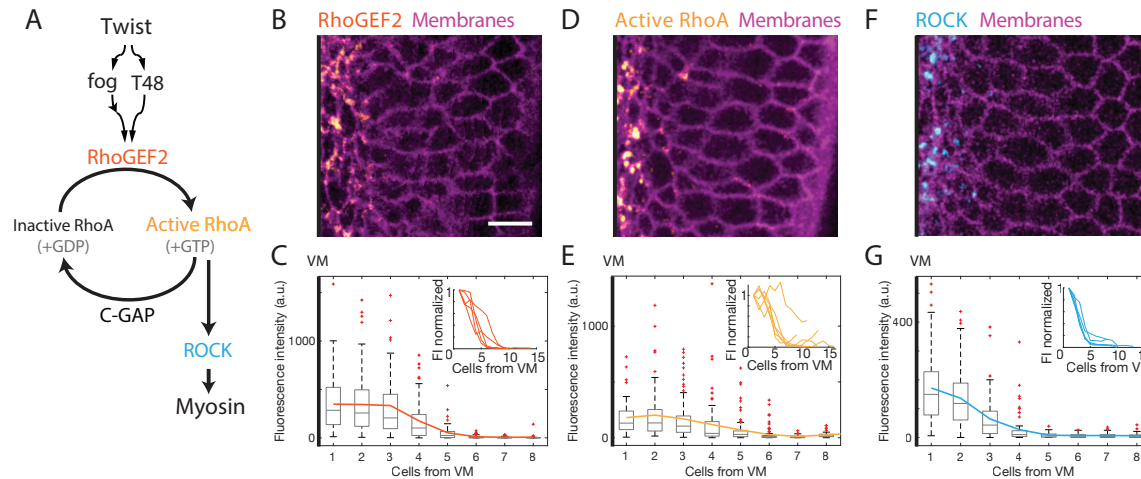
Figure 3. RhoA activation occurs in a gradient. (**A**) Simplified diagram of signaling

downstream of Twist, focused on RhoA regulation. (**B**) Image of RhoGEF2::GFP (orange)

and Gap43::mCherry (magenta). Ventral midline on left. Scale bar = 10 μm. (**D**) Image of

Anillin Rho-binding domain::GFP (yellow) and Gap43::mCherry (magenta). Ventral midline

on left. (**F**) Image of Rok::GFP (cyan) and Gap43::mCherry (magenta). Ventral midline on

left. (**C, E, G**) Apical RhoGEF2::GFP intensity (orange, **C**), Anillin Rho-binding domain::GFP

intensity (yellow, **E**), and Rok::GFP intensity (cyan, **G**) as a function of distance from the

ventral midline for one representative embryo, respectively. Data is represented by box-and-

whisker plots where each bin is a cell row at a given distance from the ventral midline.

Bottom and top sides of the box represent 25th and 75th percentile, respectively. Midline is

the median and red points are outliers. At least 32 cells (RhoGEF2, median 85 cells), 58

cells (Active RhoA, median 76.5 cells), or 51 cells (ROCK, median 68.5 cells) were analyzed

for each cell row, respectively. Insets shows average cell behavior from 5 embryos per

condition.

777
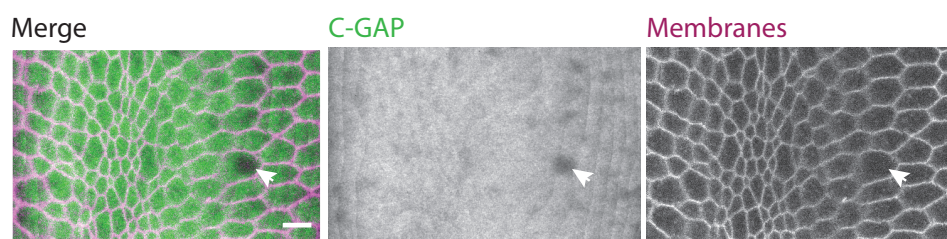
778

779   **Supplement to Figure 3.** C-GAP is uniformly cytoplasmic across the ventral furrow. Apical

780   shell projection of an embryo expressing GFP::C-GAP (green) and gap43::mCherry

781   (membranes, magenta). White arrow indicates apical nucleus with no GFP::C-GAP signal.
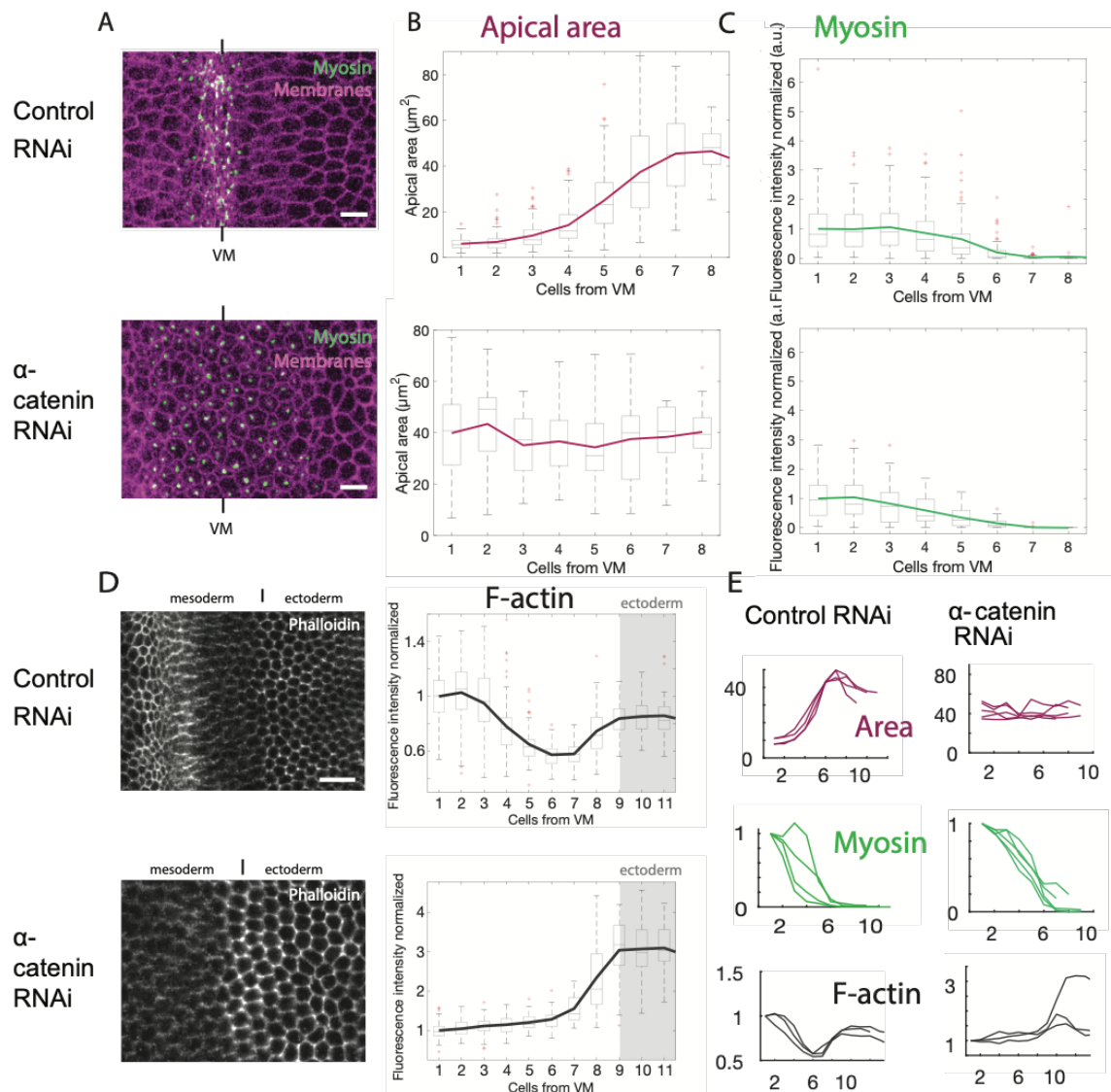
782   Scale bar = 10 μm.

783

784

Figure 4. Myosin gradient and uniform F-actin depletion do not require intercellular coupling.
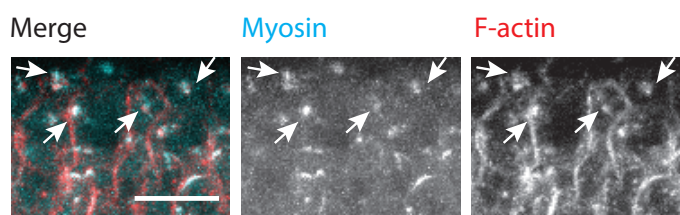
(**A**) Images (apical shell projections) of control (Rh3-RNAi) and α-catenin-RNAi embryos

expressing sqh::GFP (Myosin, green) and Gap43::mCherry (Membranes, magenta). Scale

bar = 10 μm. (**B**) and (**C**) Quantification of apical area (magenta, **B**) and normalized apical,

active myosin (green, **C**) as a function of distance from ventral midline. Data is represented

by box-and-whisker plots where each bin is a cell row at a given distance from the ventral

midline (at least 41 (control) or 44 (α-catenin-RNAi) cells per row analyzed, respectively;

median 72 (control) or 107 (α-catenin-RNAi) cells). Bottom and top sides of the box

represent 25th and 75th percentile, respectively. Midline is the median and red points are

794   outliers. (**D**) Left: Images of phalloidin-stained control (Rh3-RNAi, top) and α-catenin-RNAi

795   (bottom) embryos focused on the mesoderm-ectoderm boundary. Scale bar = 10 µm. Right:

796   Quantification of normalized cortical F-actin levels in rows of cells along the ventral-lateral

797   axis (at least 52 (control) or 8 (α-catenin-RNAi) cells per row analyzed, respectively; median

798   78 (control) or 40.5 (α-catenin-RNAi) cells). Data is represented by box-and-whisker plots

799   where each bin is a cell row at a given distance from the ventral midline. Bottom and top

800   sides of the box represent 25th and 75th percentile, respectively. Midline is the median and

801   red points are outliers. (**E**) Individual mean traces for multiple control and α-catenin-RNAi

802   embryos. Top: Average apical area behavior from 4 (control) and 5 (and α-catenin-RNAi)

803   different embryos, respectively. Mid: Average active myosin behavior from 4 (control) and 5

804   (and α-catenin-RNAi) different embryos, respectively. Bottom: Average cortical actin

805   behavior from 3 different embryos, respectively

806

807
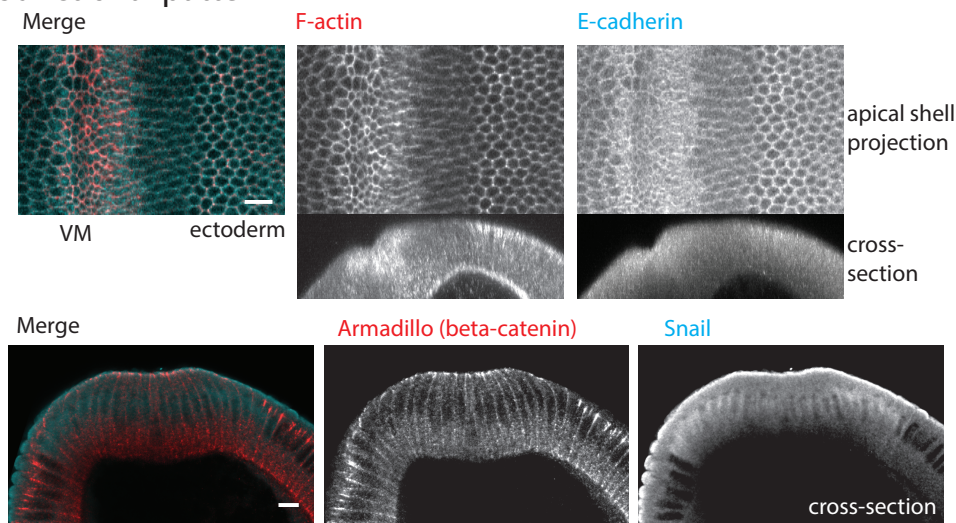
Supplement to Figure 4: F-actin is colocalized with junctions in wild-type and with medioapical myosin spots in α -catenin-RNAi embryos. (**A**) Top: Apical shell projection and cross-section (maximum intensity projection of 20 μm) images of fixed control (Rh3-RNAi) embryo stained with phalloidin (red) and anti-E-cadherin antibody (cyan). Bottom: Cross-section images of control (Rh3-RNAi) embryo stained with anti-armadillo (ß-catenin) antibody (red) and anti-Snail antibody (cyan, marking the mesoderm). Note that transition from low to high F-actin at ectoderm boundary matches adherens junction intensity transition. Scale bars = 10 μm. (**B**) Images of ventral apical surface of fixed embryo expressing sqh::GFP (Myosin light chain marker), stained with phalloidin (red) and anti-GFP (cyan) antibody. White arrows indicate medioapical spots in which myosin and F-actin are colocalized. Scale bar = 10 μm.
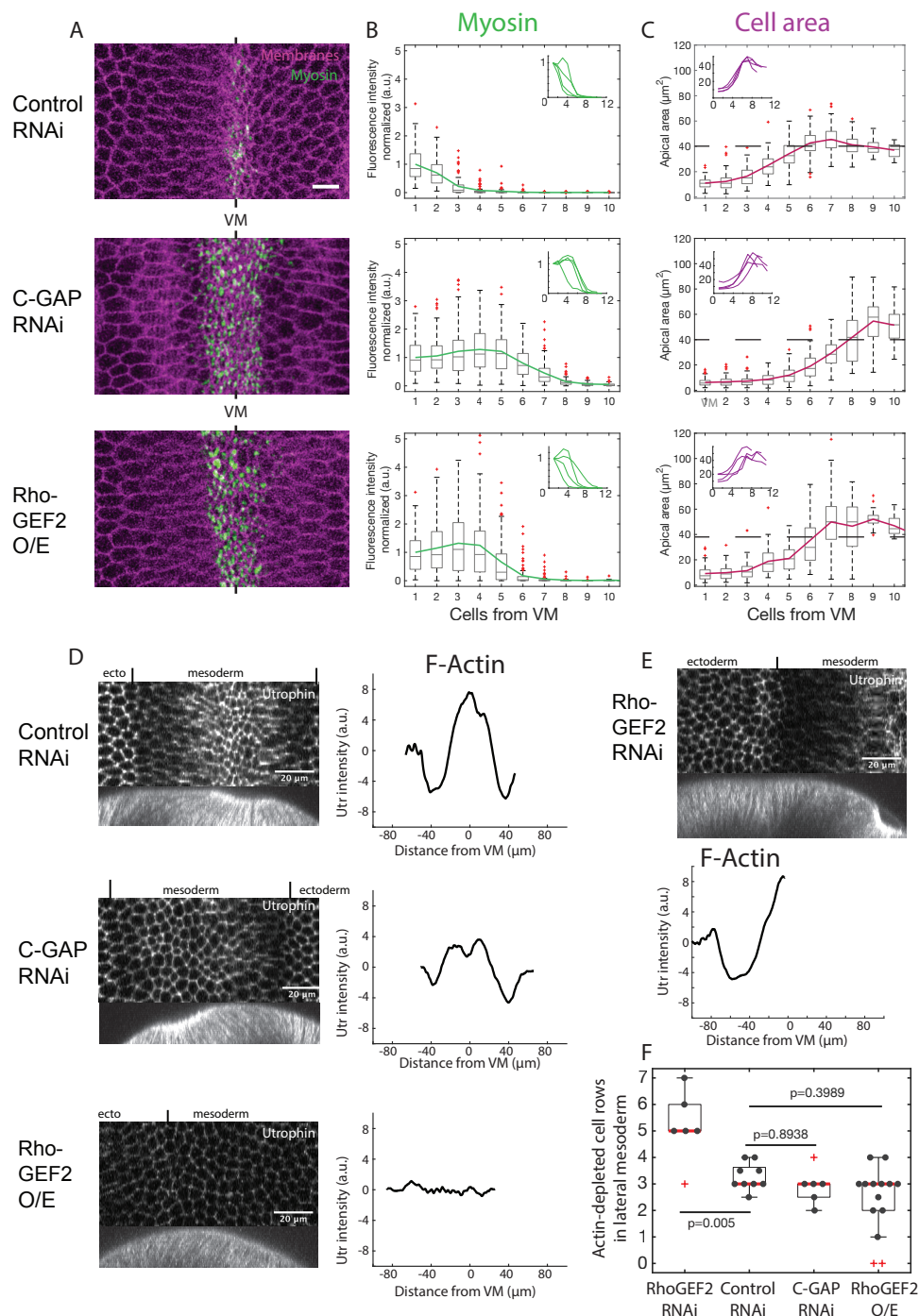
819

820

Figure 5: RhoA overactivation widens actomyosin gradient and narrows F-actin depleted

zone. (**A**) Images (apical shell projections) of control (Rh3-RNAi), C-GAP-RNAi and

RhoGEF2 O/E embryos expressing sqh::GFP (Myosin, green) and Gap43::mCherry

(Membranes, magenta). Scale bar = 10 µm. (**B**) and (**C**) Quantification of normalized apical,

active myosin (green, **B**) and apical area (magenta, **C**) as a function of distance from ventral

826   midline. Data is represented by box-and-whisker plot where each bin is a cell row at a given

827   distance from the ventral midline (at least 27 (control), 50 (C-GAP-RNAi) or 23 (RhoGEF2

828   O/E) cells per row analyzed, respectively; median 85 (control), 108.5 (C-GAP-RNAi) or 85

829   (RhoGEF2 O/E) cells). Bottom and top sides of the box represent 25th and 75th percentile,

830   respectively. Midline is the median and red points are outliers. Insets show 4 embryos for

831   each condition. (**D**) Width of F-actin depleted zone is narrower in C-GAP-RNAi and

832   RhoGEF2 O/E embryos. Left: Images (Top, subapical shell projection, and Bottom, 20 µm

833   maximum intensity projection of cross-section) of control (Rh3-RNAi), C-GAP-RNAi and

834   RhoGEF2 O/E embryos expressing Utrophin::GFP. Scale bars = 20 µm. Right:

835   Quantification of cortical F-actin levels by physical distance along the ventral-lateral axis.

836   Data is represented as mean intensity for one representative embryo. (**E**) Width of F-actin

837   depleted zone is wider in RhoGEF2-RNAi embryo. Top: Images (subapical shell projection

838   (top), and 20 µm maximum intensity projection of cross-section (below)) of RhoGEF2-RNAi

839   embryo expressing Utrophin::GFP. Scale bar = 20 µm. Bottom: Quantification of cortical F-

840   actin levels by physical distance along the ventral-lateral axis for one RhoGEF2-RNAi

841   embryo. (**F**) Width of F-actin depleted zone in cell rows for RhoGEF2-RNAi, control (Rh3-

842   RNAi), C-GAP-RNAi and RhoGEF2 O/E embryos. Data is represented by box-and-whisker

843   plot overlaid with data points for each analyzed embryo. Bottom and top sides of the box

844   represent 25th and 75th percentile, respectively. Midline is the median and red '+' are outliers.

845

846
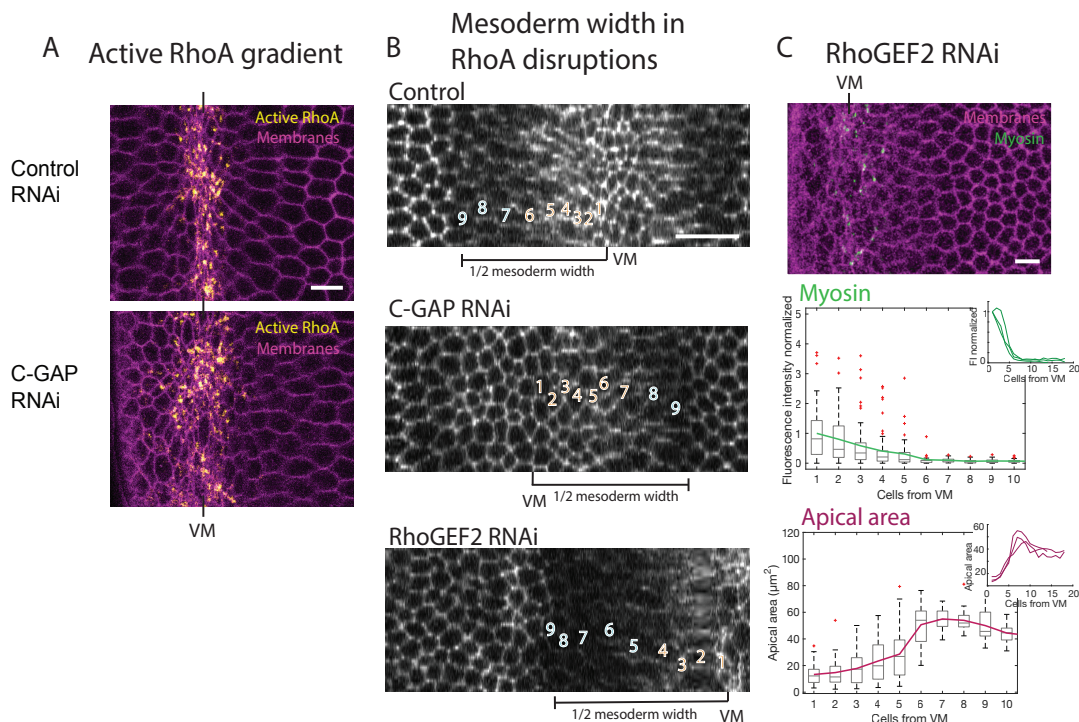
Supplement to Figure 5: RhoA and actomyosin gradient width, but not mesoderm width, are affected by RhoA regulators. (**A**) Images (apical shell projection) of control (Rh3-RNAi) and C-GAP-RNAi embryos expressing Anillin Rho-binding domain::GFP (active RhoA, yellow) and Gap43::mCherry (Membranes, magenta). Scale bar = 10 µm. (**B**) Subapical shell projections of embryos expressing Utrophin::GFP, indicating number of cell rows from the ventral midline to the mesoderm border (as visualized by change in F-actin level) for different genotypes (~9 cell rows). Cell rows with blue numbers are within the F-actin depleted zone and cell rows with orange numbers are within the F-actin gradient around the ventral midline. Scale bars = 20 µm. (**C**) Top: Image (apical shell projection) of RhoGEF2-RNAi embryo expressing sqh::GFP (Myosin, green) and Gap43::mCherry (Membranes, magenta). Scale bar = 10 µm. Bottom: Quantification of apical area (magenta) and normalized apical, active myosin (green) as a function of distance from ventral midline (at least 23 cells per cell row were analyzed; median 38 cells). Data is represented by box-and-whisker plot where each bin is a cell row at a given distance from the ventral midline. Bottom, and top, sides of the box represent 25th and 75th percentile of cells, respectively.

862   Midline is the median and red '+' are outliers. Inset shows average cell behavior from 3
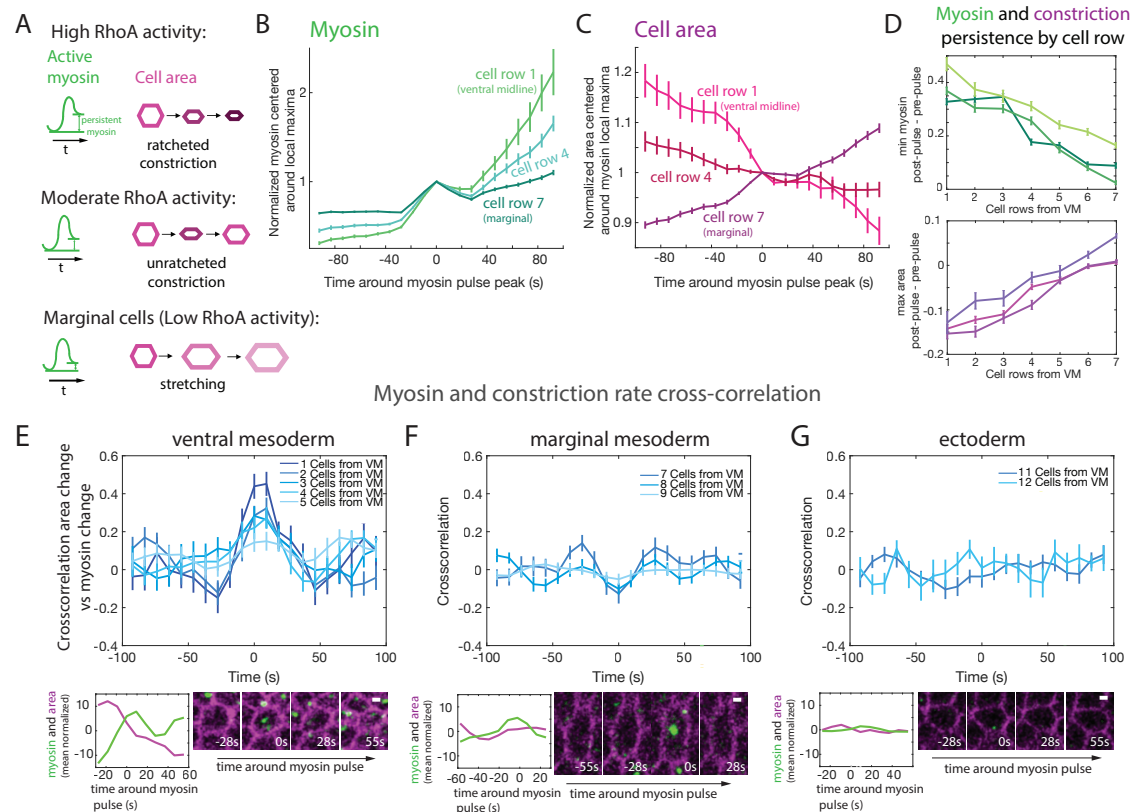
863   different embryos.

864

Figure 6: Contractile dynamics vary with ventral-lateral cell position. (**A**) There are distinct types of dynamic cell behaviors during ventral furrow formation. Top: When RhoA activity is high, cells preferably undergo "ratcheted" myosin pulses after which myosin increases and apical area is sustained. Middle: At moderate RhoA activity, cells undergo myosin pulses in which myosin and apical area reverse after contraction. Bottom: In marginal mesoderm cells, myosin pulses occur while the apical cell surface stretches, but the relationship of myosin and stretching dynamics was not understood. (**B**) Myosin persistence is highest close to the ventral midline. Average and standard error of myosin levels during and after a myosin pulse (local maxima in myosin accumulation rate) for cell row 1 at the midline (light green), intermediate cell row 4 (mint) and marginal mesoderm cell row 7 (dark green) shown for one representative embryo. 106 pulses were analyzed for cell row 1; 192 pulses were analyzed for cell row 4; 335 pulses were analyzed for cell row 7. (**C**) Myosin pulses away from the midline are associated with stretching. Average and standard error of apical area dynamics around pulses (local maxima in constriction rate) for cell row 1 at the midline (light magenta),

879   intermediate cell row 4 (maroon) and marginal mesoderm cell row 7 (dark magenta) shown

880   for one representative embryo. 106 pulses were analyzed for cell row 1; 192 pulses were

881   analyzed for cell row 4; 335 pulses were analyzed for cell row 7. (**D**) Average and standard

882   error for persistence of myosin (minimum myosin 0-100 s after pulse - minimum myosin 0-

883   100 s before pulse) and area (maximum area 0-100 s after pulse - maximum area 0-100 s

884   before pulse) by bin (distance from the midline) for three embryos. At least 83 pulses were

885   analyzed for each cell row in each embryo. Median 192, 238 and 343 pulses analyzed per

886   cell row for the three embryos, respectively. (**E**)-(**F**) Top: Cross-correlation between the rate

887   of change in apical myosin intensity (normalized to apical area) and constriction rate

888   averaged by cell bin; split up by ventral mesoderm (cell rows 1-5, **E**), marginal mesoderm

889   (cell rows 7-9, **F**) and ectoderm (cell rows 11 and 12, **G**). At least 21 cells per cell row were

890   analyzed, median 32 cells per cell row. Bottom: Myosin (green) and apical area (magenta)

891   traces (normalized to average) and images of representative individual cells during a myosin

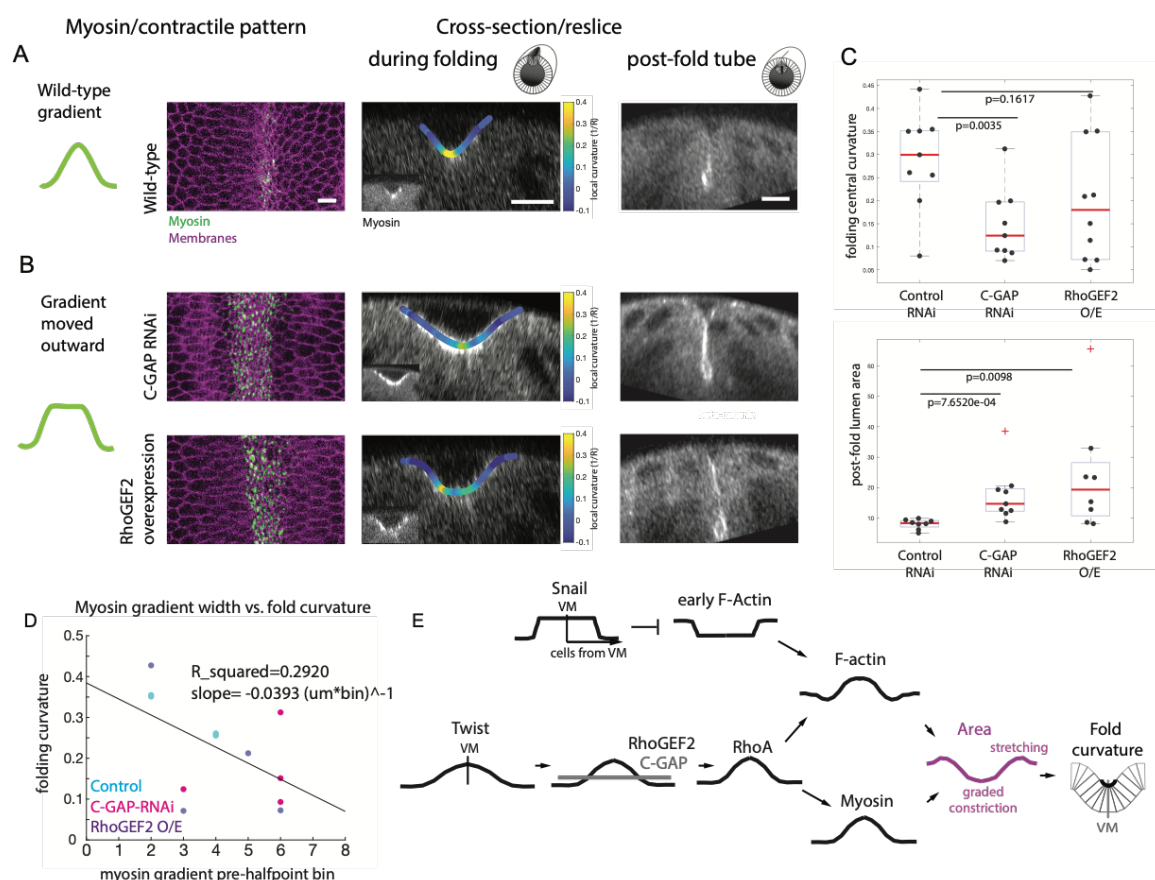892   pulse, for each region. Scale bars = 2 μm.

893

894

895

896 **Figure 7:** The contractile pattern determines fold curvature and post-fold shape. (**A**)

897 Subapical shell projection and later cross-sections during and after folding of a single control

898 (Rh3-RNAi) embryo expressing sqh::GFP (myosin) and gap43::mCh (membranes). In

899 control embryos, in which the actomyosin gradient extends from cells 2-5, the ventral-lateral

900 cross-section shows a narrow, v-shaped fold with high curvature at the center (local

901 curvature is color-coded on the surface of the fold). The cross-sectional view of this embryo

902 after folding shows a tube with a very small lumen. Scale bars = 10 μm. (**B**) Subapical shell

903 projections and cross-sections during and after folding of a single C-GAP-RNAi embryo (top)

904 and a single RhoGEF2 O/E embryo (bottom), expressing sqh::GFP (myosin) and

905 gap43::mCh (membranes). C-GAP-RNAi and RhoGEF2 O/E embryos, which have a

906 widened gradient with uniform myosin at the ventral midline display lower central fold

907 curvature (local curvature is color-coded on the surface of the fold). At later timepoints, they

908 often have an enlarged tube lumen as outlined by myosin signal in cross-section. (**C**)

909   Quantification of curvature at the center of the fold (measured by fitting a circle, 3

910   measurements at different AP positions averaged per embryo) (top) and lumen size

911   (measured by fitting an ellipse) (bottom) for control (Rh3-RNAi), C-GAP-RNAi and RhoGEF2

912   O/E embryos. Data is represented by box-and-whisker plot overlaid with data points

913   representing each quantified embryo. Bottom and top sides of the box represent 25th and

914   75th percentile of embryos, respectively. Midline is the median and red '+' are outliers. (**D**)

915   Regression analysis of the relationship between myosin gradient width and curvature for

916   control, C-GAP-RNAi and RhoGEF2 O/E embryos. Gradient width was measured as the cell

917   row bin that was just above the half-maximal intensity of the myosin gradient. Curvature was

918   measured as in (C). (**E**) Model for the regulation of tissue-wide patterning in the ventral

919   furrow. Uniform *snail* expression causes uniform F-actin depletion in the mesoderm. An

920   overlapping pattern of graded *twist* expression acts via tightly tuned RhoA activation to

921   generate an actomyosin gradient. Folding is driven by the combination of ventral midline cell

922   actomyosin contractility and stretching of marginal mesoderm cells, which are depleted of F-

923   actin.

924

925
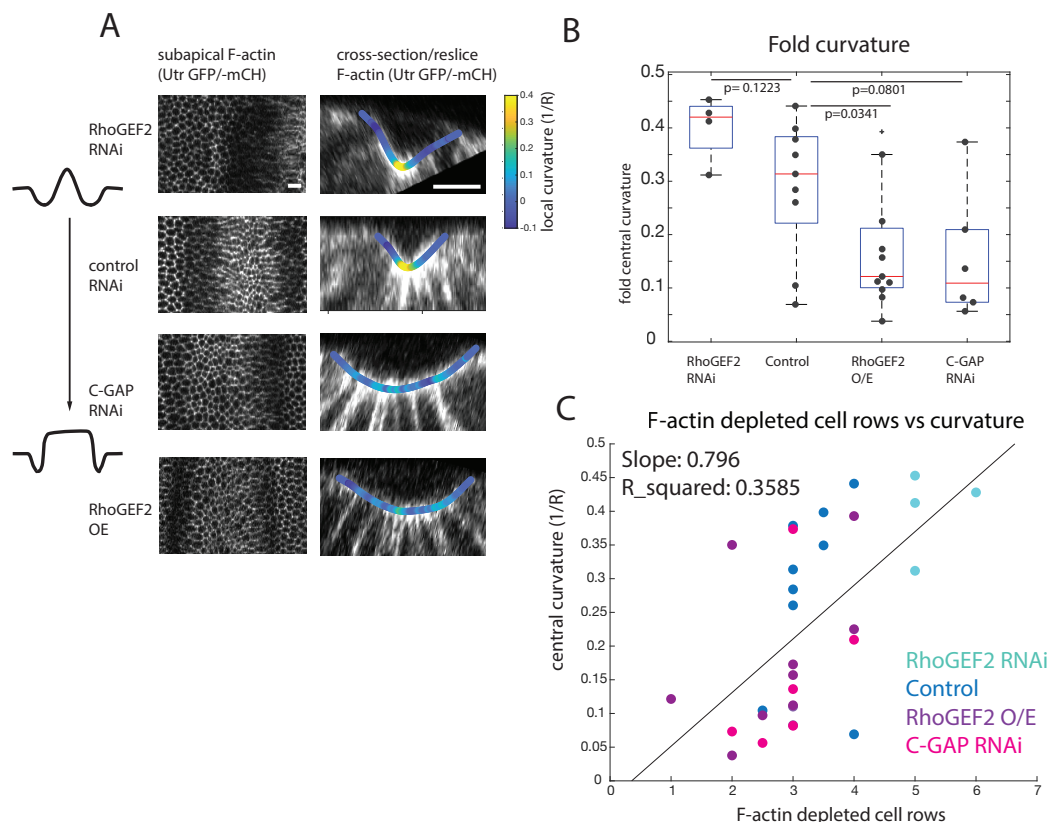
Supplement to Figure 7: The width of the F-actin depletion zone is correlated with fold

curvature. (**A**) Subapical shell projections during early folding (left) and cross-sections (right)

later during folding for single RhoGEF2-RNAi, control (Rh3-RNAi), C-GAP-RNAi and

RhoGEF2 O/E embryos expressing Utrophin-GFP. In cross-section, local curvature is color-

coded on the surface of the fold. Scale bars = 10 μm. (**B**) Quantification of curvature at the

center of the fold (measured by fitting a circle, three measurements averaged per embryo)

for RhoGEF2-RNAi, control (Rh3-RNAi), C-GAP-RNAi and RhoGEF2 O/E embryos. Data is

represented by box-and-whisker plot overlaid with data points from all quantified embryos.

Bottom, and top sides, of the box represent 25th and 75th percentile, respectively. Midline is

the median and black '+' are outliers. (**C**) Regression analysis of the relationship between F-

actin depleted region width and curvature for RhoGEF2-RNAi, control, C-GAP-RNAi and

RhoGEF2 O/E embryos. Depleted F-actin region width was determined by the number of cell

rows with low F-actin intensity. Curvature was measured as in (B).

939

940

941 **Supplemental Movie S1 (related to Figure 4).** Shell-projection (with background

942 subtraction and gaussian blur) of control (Rh3-RNAi) embryo expressing sqh::GFP (myosin,

943 green) and gap43::mCh (membranes, magenta) during ventral furrow formation. t=0

944 corresponds to the timepoint analyzed in Figure 4. Time step = 43.29 s, Frame rate = 2.5/s.

945

946 **Supplemental Movie S2 (related to Figure 4).** Shell-projection (with background

947 subtraction and gaussian blur) of α-catenin-RNAi embryo expressing sqh::GFP (myosin,

948 green) and gap43::mCh (membranes, magenta) trying to initiate ventral furrow formation. t=0

949 corresponds to the timepoint analyzed in Figure 4. Time step = 21.94 s, Frame rate = 5/s.

950

951 **Supplemental Movie S3 (related to Figure 7).** Maximum intensity projection of control

952 (Rh3-RNAi) embryo expressing sqh::GFP (myosin, green) and gap43::mCh (membranes,

953 magenta), during and after ventral furrow formation (gaussian blur radius =1). Time step =

954 53.653 s, Frame rate = 3.1/s.

955

956

957 **Supplemental Movie S4 (related to Figure 7).** Maximum intensity projection of RhoGEF2-

958 RNAi embryo expressing sqh::GFP (myosin, green) and gap43::mCh (membranes,

959 magenta), during and after ventral furrow formation (gaussian blur radius =1). Note divisions

960 of mitotic domain 10 visible at the embryo surface after folding. Time step = 73.643 s, Frame

961 rate = 4/s.

962

963

964

965

966 **Supplemental table S1.** Fly Stocks and crosses used in this study:

Stock	Genotype	Source/Reference	Figure
1	w; Gap43::mCherry(attp40); Sqh::GFP	Martin et al., 2010	
2	y, w[67c], sqh[AX3], cv; Sqh::GFP[42]	Bloomington Drosophila Stock Center	
3	OreR	Bloomington Drosophila Stock Center	1B-E, S1A, 2A
4	y[1] sc[*] v[1]; P{y[+t7.7] v[+t1.8]=TRiP.GL01052}attP2 (Rh3 shRNA control line)	Perkins et al., 2015	
5	w; mat67; mat15	Vasquez et al., 2014	
6	UtrABD-GFP;+	Rauzi et al. 2010	
7	w; gap43::mCherry/TM3, Sb[1]	Bardet et al. 2013	
8	Halo-sna/CyO-sqhGFP	Martin et al., 2009	
9	halo, twist[ey53] /CyO, Sqh::GFP	Martin et al., 2009	
10	UtrABD-mCH	Rauzi et al. 2010	
11	y w hs-flp; FRT42BG13 RhoGEF2[1.1]/CyO; GFP::Rhogef2 BAC(VK33)	Mason et al. 2016	
12	w[1118]; Df(2R)ED2747, P{w[+mW.Scer\FRT.hs3]=3'.RS5+3.3'}ED2747/SM6a; GFP::Rho	Mason et al. 2016	
13	Ubi-AniRBD-GFP; gap43mCH	This study (original Ubi>AniRBD-GFP stock: Munjal et al. 2015)	
14	Ubi-RokGFP; gap43mCh	Bardet et al. 2013	
15	w; mat67, Sqh::GFP; mat15, Gap43::mCherry/(TM3, Sb[1])	Vasquez et al., 2014	
16	Alpha-catenin RNAi (HMS), sqh-GFP	This study	
17	Alpha-catenin RNAi (HMS)	Perkins et al., 2015	
18	sqhGFP; P{y[+t7.7] v[+t1.8]=TRiP.GL01052}attP2 (Rh3 shRNA control line)	this study	
19	sqhGFP; P{TRiP.HMS00412}attP2 (RhoGAP71E, C-GAP shRNA)	This study	
20	y[1] w[*]; P{UASp-T7.RhoGEF2}5 (RhoGEF2 overexpression line)	Bloomington Drosophila Stock Center	
21	y,w; Sqh::GFP; mat15, Gap43::mCherry/(TM3, Sb[1])	Vasquez et al., 2014	
22	y[1] sc[*] v[1]; P{TRiP.HMS00412}attP2 (*RhoGAP71E, C-GAP shRNA*)	Perkins et al., 2015	
23	Mat 67, UtrABD-GFP	Jodoin and Martin, 2016	
24	mat15, Utr::GFP; sqhmCH	This study	
25	mat15, Utr::mCh	This study	
26	y[1] sc[*] v[1]; P{TRiP.HMS01118}attP2 (*RhoGEF2 shRNA*)	Perkins et al., 2015	
27	Ubi-AniRBD-GFP; 71E HMS	This study	
28	Ubi-AniRBD-GFP; RH3GL	this study	
29	mat67; mat15, gap43::mCh	Vasquez et al., 2014	
30	y,w;+;C-GAP-GFP	This study	1B, S3A

F2 embryos imaged from these crosses, using above stock numbers/genotypes. Non-balancer females were used for cages.		
Stock # 1 x 2 (Virgins x males)		1A, 6
4x5		4D, S4A
6x7		S1
8x6		2B,C
8x10		2B, C
8x6		2D,E
9x10		2D,E
11x12		3B,C
13x3		3D, E
14x3		3F,G
4x15		4A-C,E, 5A-C, 7A,C,D
18x15		4A-C,E, 5A-C, 6B-G
16x15		4A-C,E
17x5		4D-E, S4B
4x21		5A-C, 7B-D
19x15		5A-C, S6A,B, 7B-D
20x21	cages kept at RT >24h before imaging	5A-C, 7B-D
4x23		5D,F, S5C, S7A-C
22x23		5D,F, S5C, S7A-C
20x24	cages kept at RT >24h before imaging	5D,F, S7A-C
20x23	cages kept at RT >24h before imaging	5D,F, S7A-C
20x25	cages kept at RT >24h before imaging	5D,F, S7A-C
26x23	cages kept at RT >24h before imaging	5E,F, S5C, S7A-C
27x29		S5A
28x29		S5A
26x 21	cages kept at RT >24h before imaging	S5B

967

References:
Bardet, P. L., B. Guirao, C. Paoletti, F. Serman, V. Léopold, F. Bosveld, Y. Goya, V. Mirouse, F. Graner, and Y. Bellaïche. 2013. PTEN controls junction lengthening and stability during cell rearrangement in epithelial tissue. *Dev. Cell*. 25:534–546.
Chanet, S., Miller, C. J., Vaishnav, E. D., Ermentrout, B., Davidson, L. A., & Martin, A. C. (2017). Actomyosin meshwork mechanosensing enables tissue shape to orient cell force. *Nature Communications*, 8, 15014. https://doi.org/10.1038/ncomms15014
Jodoin, J. N., & Martin, A. C. (2016). Abl suppresses cell extrusion and intercalation during epithelium folding. *Molecular Biology of the Cell*, 27 (18), 2822–2832. https://doi.org/10.1091/mbc.E16-05-0336
Martin, A. C., M. Gelbart, R. Fernandez-Gonzalez, M. Kaschube, and E. F. Wieschaus. 2010. Integration of contractile forces during tissue invagination. *J. Cell Biol*. 188:735–749.
Martin, A. C., M. Kaschube, and E. F. Wieschaus. 2009. Pulsed contractions of an actin-myosin network drive apical constriction. *Nature*. 457:495–499.
Mason, F. M., Xie, S., Vasquez, C. G., Tworoger, M., & Martin, A. C. (2016). RhoA GTPase inhibition organizes contraction during epithelial morphogenesis. *The Journal of Cell Biology*, 214 (5). Retrieved from http://jcb.rupress.org/content/214/5/603.long
Munjal, A., J.-M. Philippe, E. Munro, and T. Lecuit. 2015. A self-organized biomechanical network drives shape changes during tissue morphogenesis. *Nature*. 524:351–355.
Perkins, L. A., L. Holderbaum, R. Tao, Y. Hu, R. Sopko, K. McCall, D. Yang-Zhou, I. Flockhart, R. Binari, H.-S. Shim, et al. 2015. The Transgenic RNAi Project at Harvard Medical School: resources and validation. *Genetics*. 201:843–852.
Rauzi, M., Lenne, P. F., & Lecuit, T. (2010). Planar polarized actomyosin contractile flows control epithelial junction remodelling. *Nature*. https://doi.org/10.1038/nature09566
Vasquez, C. G., M. Tworoger, and A. C. Martin. 2014. Dynamic myosin phosphorylation regulates contractile pulses and tissue integrity during epithelial morphogenesis. *J. Cell Biol*. 206:435–450.

968

969 **Supplemental Table S2.** Imaging settings used in this study:

Imaging settings

Fluorescent tag combination	Figures	Excitation laser wavelength	Detector start wavelength (nm)	Detector end wavelength (nm)	Detector Gain (a.u.)	Laser power (%)	Pinhole size (x10^(-4) m)
sqh::GFP (Myosin)	1A, 4A-C, S4C, 5A, S5b, 6, S6, 7	488	493	537.57 to 586	700 to 874.081	2 to 7	76.545 to 89.944
gap43mCh (Membranes)	1A, S1B, 3, S3, 4A-C, S4C, 5A, S5A+B, 6, S6, 7	561	569.57 to 603.82	696 to 698.26	763 to 866	2 to 6.5	76.545 to 89.944
		594	600.32 to 614.82	696	840-856	5-6.5	
Utrophin::GFP	S1B, 2B,C, 5D-F, S5C, S7	488	493	562.07 to 598	770-850	2 to 4	89.944
Utrophin::mCh	2B-E, 5D-F, S7	561	578	696	770-800	4.3 to 5	89.944
RhoGEF2::GFP	3B	488	493	561	850	12	89.944
Anillin::GFP+[Imagingsettings..	3C	488	493	561	850	12 to 22	89.944
Rok-GFP	3D	488	493	561	850	7	89.944
C-GAP-GFP	S3	488	493	565	900	16	89.214
Phalloidin Alexa Fluor 568	1B-D, S1A, 4D, S4A, B	561	569 to 574	647 to 712	600 to 700	1 to 2	37.175 to 77.853
Alexa Fluor 488 secondary antibody	S1A (snail), 2A (snail), S4A (armadillo)	488	493	574	500-600	2	45.511 or 89.213
Alexa Fluor 647 secondary antibody	S4A (ecadherin)	633	647	755	800	5	42.175
Alexa Fluor 568 secondary antibody	S4A (Snail)	568	574	712	600	1.2	89.213
sqhGFP fixed	S4A	488	493	569	800	8	37.175

970

References

Bailles, A., C. Collinet, J.M. Philippe, P.F. Lenne, E. Munro, and T. Lecuit. 2019. Genetic induction and mechanochemical propagation of a morphogenetic wave. *Nature*. 572:467-473.

Barrett, K., M. Leptin, and J. Settleman. 1997. The Rho GTPase and a putative RhoGEF mediate a signaling pathway for the cell shape changes in Drosophila gastrulation. *Cell*. 91:905-915.

Boulay, J.L., C. Dennefeld, and A. Alberga. 1987. The Drosophila developmental gene snail encodes a protein with nucleic acid binding fingers. *Nature*. 330:395-398.

Chanet, S., C.J. Miller, E.D. Vaishnav, B. Ermentrout, L.A. Davidson, and A.C. Martin. 2017. Actomyosin meshwork mechanosensing enables tissue shape to orient cell force. *Nat Commun*. 8:15014.

Chanet, S., and F. Schweisguth. 2012. Regulation of epithelial polarity by the E3 ubiquitin ligase Neuralized and the Bearded inhibitors in Drosophila. *Nat Cell Biol*. 14:467-476.

Costa, M., E.T. Wilson, and E. Wieschaus. 1994. A putative cell signal encoded by the folded gastrulation gene coordinates cell shape changes during Drosophila gastrulation. *Cell*. 76:1075-1089.

Dawes-Hoang, R.E., K.M. Parmar, A.E. Christiansen, C.B. Phelps, A.H. Brand, and E.F. Wieschaus. 2005. folded gastrulation, cell shape change and the control of myosin localization. *Development*. 132:4165-4178.

Denk-Lobnig, M., and A.C. Martin. 2019. Modular regulation of Rho family GTPases in development. *Small GTPases*. 10:122-129.

Fernandez-Gonzalez, R., and J.A. Zallen. 2011. Oscillatory behaviors and hierarchical assembly of contractile structures in intercalating cells. *Phys Biol*. 8:045005.

Foe, V.E. 1989. Mitotic domains reveal early commitment of cells in Drosophila embryos. *Development*. 107:1-22.

Fox, D.T., and M. Peifer. 2007. Abelson kinase (Abl) and RhoGEF2 regulate actin organization during cell constriction in Drosophila. *Development*. 134:567-578.

Furlong, E.E., E.C. Andersen, B. Null, K.P. White, and M.P. Scott. 2001. Patterns of gene expression during Drosophila mesoderm development. *Science*. 293:1629-1633.

Fuse, N., F. Yu, and S. Hirose. 2013. Gprk2 adjusts Fog signaling to organize cell movements in Drosophila gastrulation. *Development*. 140:4246-4255.

Gelbart, M.A., B. He, A.C. Martin, S.Y. Thiberge, E.F. Wieschaus, and M. Kaschube. 2012. Volume conservation principle involved in cell lengthening and nucleus movement during tissue morphogenesis. *Proc Natl Acad Sci U S A*. 109:19298-19303.

Gratz, S.J., M.M. Harrison, J. Wildonger, and K.M. O'Connor-Giles. 2015. Precise Genome Editing of Drosophila with CRISPR RNA-Guided Cas9. *Methods Mol Biol*. 1311:335-348.

Gratz, S.J., F.P. Ukken, C.D. Rubinstein, G. Thiede, L.K. Donohue, A.M. Cummings, and K.M. O'Connor-Giles. 2014. Highly specific and efficient CRISPR/Cas9-catalyzed homology-directed repair in Drosophila. *Genetics*. 196:961-971.

Grosshans, J., and E. Wieschaus. 2000. A genetic link between morphogenesis and cell division during formation of the ventral furrow in Drosophila. *Cell*. 101:523-531.

Hacker, U., and N. Perrimon. 1998. DRhoGEF2 encodes a member of the Dbl family of oncogenes and controls cell shape changes during gastrulation in Drosophila. *Genes Dev*. 12:274-284.

1019 Heer, N.C., P.W. Miller, S. Chanet, N. Stoop, J. Dunkel, and A.C. Martin. 2017.
1020   Actomyosin-based tissue folding requires a multicellular myosin gradient.
1021   *Development*. 144:1876-1886.
1022 Homem, C.C., and M. Peifer. 2008. Diaphanous regulates myosin and adherens junctions to
1023   control cell contractility and protrusive behavior during morphogenesis. *Development*.
1024   135:1005-1018.
1025 Hong, L., M. Dumond, S. Tsugawa, A. Sapala, A.L. Routier-Kierzkowska, Y. Zhou, C. Chen,
1026   A. Kiss, M. Zhu, O. Hamant, R.S. Smith, T. Komatsuzaki, C.B. Li, A. Boudaoud, and
1027   A.H. Roeder. 2016. Variable Cell Growth Yields Reproducible OrganDevelopment
1028   through Spatiotemporal Averaging. *Dev Cell*. 38:15-32.
1029 Iseli, C., G. Ambrosini, P. Bucher, and C.V. Jongeneel. 2007. Indexing strategies for rapid
1030   searches of short words in genome sequences. *PLoS One*. 2:e579.
1031 Jha, A., T.S. van Zanten, J.M. Philippe, S. Mayor, and T. Lecuit. 2018. Quantitative Control
1032   of GPCR Organization and Signaling by Endocytosis in Epithelial Morphogenesis.
1033   *Curr Biol*. 28:1570-1584 e1576.
1034 Jodoin, J.N., J.S. Coravos, S. Chanet, C.G. Vasquez, M. Tworoger, E.R. Kingston, L.A.
1035   Perkins, N. Perrimon, and A.C. Martin. 2015. Stable Force Balance between
1036   Epithelial Cells Arises from F-Actin Turnover. *Dev Cell*. 35:685-697.
1037 Kerridge, S., A. Munjal, J.M. Philippe, A. Jha, A.G. de las Bayonas, A.J. Saurin, and T.
1038   Lecuit. 2016. Modular activation of Rho1 by GPCR signalling imparts polarized
1039   myosin II activation during morphogenesis. *Nat Cell Biol*. 18:261-270.
1040 Ko, C.S., P. Kalakuntla, and A.C. Martin. 2020. Apical Constriction Reversal upon Mitotic
1041   Entry Underlies Different Morphogenetic Outcomes of Cell Division. *Mol Biol
1042   Cell*:mbcE19120673.
1043 Kolsch, V., T. Seher, G.J. Fernandez-Ballester, L. Serrano, and M. Leptin. 2007. Control of
1044   Drosophila gastrulation by apical localization of adherens junctions and RhoGEF2.
1045   *Science*. 315:384-386.
1046 Latorre, E., S. Kale, L. Casares, M. Gomez-Gonzalez, M. Uroz, L. Valon, R.V. Nair, E.
1047   Garreta, N. Montserrat, A. Del Campo, B. Ladoux, M. Arroyo, and X. Trepat. 2018.
1048   Active superelasticity in three-dimensional epithelia of controlled shape. *Nature*.
1049   563:203-208.
1050 Leptin, M. 1991. twist and snail as positive and negative regulators during Drosophila
1051   mesoderm development. *Genes Dev*. 5:1568-1576.
1052 Leptin, M. 2005. Gastrulation movements: the logic and the nuts and bolts. *Dev Cell*. 8:305-
1053   320.
1054 Leptin, M., and B. Grunewald. 1990. Cell shape changes during gastrulation in Drosophila.
1055   *Development*. 110:73-84.
1056 Lim, B., M. Levine, and Y. Yamazaki. 2017. Transcriptional Pre-patterning of Drosophila
1057   Gastrulation. *Curr Biol*. 27:610.
1058 Manning, A.J., K.A. Peters, M. Peifer, and S.L. Rogers. 2013. Regulation of epithelial
1059   morphogenesis by the G protein-coupled receptor mist and its ligand fog. *Sci Signal*.
1060   6:ra98.
1061 Martin, A.C., M. Gelbart, R. Fernandez-Gonzalez, M. Kaschube, and E.F. Wieschaus. 2010.
1062   Integration of contractile forces during tissue invagination. *J Cell Biol*. 188:735-749.
1063 Martin, A.C., M. Kaschube, and E.F. Wieschaus. 2009. Pulsed contractions of an actin-
1064   myosin network drive apical constriction. *Nature*. 457:495-499.
1065 Mason, F.M., M. Tworoger, and A.C. Martin. 2013. Apical domain polarization localizes
1066   actin-myosin activity to drive ratchet-like apical constriction. *Nat Cell Biol*. 15:926-
1067   936.

1068   Mason, F.M., S. Xie, C.G. Vasquez, M. Tworoger, and A.C. Martin. 2016. RhoA GTPase
1069   inhibition organizes contraction during epithelial morphogenesis. *J Cell Biol*.
1070   214:603-617.
1071   Mitrossilis, D., J.C. Roper, D. Le Roy, B. Driquez, A. Michel, C. Menager, G. Shaw, S. Le
1072   Denmat, L. Ranno, F. Dumas-Bouchiat, N.M. Dempsey, and E. Farge. 2017.
1073   Mechanotransductive cascade of Myo-II-dependent mesoderm and endoderm
1074   invaginations in embryo gastrulation. *Nat Commun*. 8:13883.
1075   Mongera, A., P. Rowghanian, H.J. Gustafson, E. Shelton, D.A. Kealhofer, E.K. Carn, F.
1076   Serwane, A.A. Lucio, J. Giammona, and O. Campas. 2018. A fluid-to-solid jamming
1077   transition underlies vertebrate body axis elongation. *Nature*. 561:401-405.
1078   Munjal, A., J.M. Philippe, E. Munro, and T. Lecuit. 2015. A self-organized biomechanical
1079   network drives shape changes during tissue morphogenesis. *Nature*. 524:351-355.
1080   Nikolaidou, K.K., and K. Barrett. 2004. A Rho GTPase signaling pathway is used
1081   reiteratively in epithelial folding and potentially selects the outcome of Rho
1082   activation. *Curr Biol*. 14:1822-1826.
1083   Perez-Mockus, G., K. Mazouni, V. Roca, G. Corradi, V. Conte, and F. Schweisguth. 2017.
1084   Spatial regulation of contractility by Neuralized and Bearded during furrow
1085   invagination in Drosophila. *Nat Commun*. 8:1594.
1086   Rahimi, N., I. Averbukh, S. Carmon, E.D. Schejter, N. Barkai, and B.Z. Shilo. 2019.
1087   Dynamics of Spaetzle morphogen shuttling in the Drosophila embryo shapes pattern.
1088   *Development*. 146:doi: 10.1242/dev.181487.
1089   Rauzi, M., U. Krzic, T.E. Saunders, M. Krajnc, P. Ziherl, L. Hufnagel, and M. Leptin. 2015.
1090   Embryo-scale tissue mechanics during Drosophila gastrulation movements. *Nat
1091   Commun*. 6:8677.
1092   Rembold, M., L. Ciglar, J.O. Yanez-Cuna, R.P. Zinzen, C. Girardot, A. Jain, M.A. Welte, A.
1093   Stark, M. Leptin, and E.E. Furlong. 2014. A conserved role for Snail as a potentiator
1094   of active transcription. *Genes Dev*. 28:167-181.
1095   Rogers, K.W., and A.F. Schier. 2011. Morphogen gradients: from generation to
1096   interpretation. *Annu Rev Cell Dev Biol*. 27:377-407.
1097   Salbreux, G., G. Charras, and E. Paluch. 2012. Actin cortex mechanics and cellular
1098   morphogenesis. *Trends Cell Biol*. 22:536-545.
1099   Schindelin, J., I. Arganda-Carreras, E. Frise, V. Kaynig, M. Longair, T. Pietzsch, S.
1100   Preibisch, C. Rueden, S. Saalfeld, B. Schmid, J.Y. Tinevez, D.J. White, V.
1101   Hartenstein, K. Eliceiri, P. Tomancak, and A. Cardona. 2012. Fiji: an open-source
1102   platform for biological-image analysis. *Nat Methods*. 9:676-682.
1103   Spahn, P., and R. Reuter. 2013. A vertex model of Drosophila ventral furrow formation.
1104   *PLoS One*. 8:e75051.
1105   Spracklen, A.J., T.N. Fagan, K.E. Lovander, and T.L. Tootle. 2014. The pros and cons of
1106   common actin labeling tools for visualizing actin dynamics during Drosophila
1107   oogenesis. *Dev Biol*. 393:209-226.
1108   Stricker, J., T. Falzone, and M.L. Gardel. 2010. Mechanics of the F-actin cytoskeleton. *J
1109   Biomech*. 43:9-14.
1110   Sui, L., S. Alt, M. Weigert, N. Dye, S. Eaton, F. Jug, E.W. Myers, F. Julicher, G. Salbreux,
1111   and C. Dahmann. 2018. Differential lateral and basal tension drive folding of
1112   Drosophila wing discs through two distinct mechanisms. *Nat Commun*. 9:4620.
1113   Sumigray, K.D., M. Terwilliger, and T. Lechler. 2018. Morphogenesis and
1114   Compartmentalization of the Intestinal Crypt. *Dev Cell*. 45:183-197 e185.
1115   Sweeton, D., S. Parks, M. Costa, and E. Wieschaus. 1991. Gastrulation in Drosophila: the
1116   formation of the ventral furrow and posterior midgut invaginations. *Development*.
1117   112:775-789.

1118   Thisse, B., C. Stoetzel, C. Gorostiza-Thisse, and F. Perrin-Schmitt. 1988. Sequence of the
1119   twist gene and nuclear localization of its protein in endomesodermal cells of early
1120   Drosophila embryos. *EMBO J.* 7:2175-2183.
1121   Ulrich, A., K.R. Andersen, and T.U. Schwartz. 2012. Exponential megapriming PCR (EMP)
1122   cloning--seamless DNA insertion into any target plasmid without sequence
1123   constraints. *PLoS One.* 7:e53360.
1124   Vasquez, C.G., M. Tworoger, and A.C. Martin. 2014. Dynamic myosin phosphorylation
1125   regulates contractile pulses and tissue integrity during epithelial morphogenesis. *J
1126   Cell Biol.* 206:435-450.
1127   von Dassow, M., and L.A. Davidson. 2009. Natural variation in embryo mechanics:
1128   gastrulation in Xenopus laevis is highly robust to variation in tissue stiffness. *Dev
1129   Dyn.* 238:2-18.
1130   Weng, M., and E. Wieschaus. 2016. Myosin-dependent remodeling of adherens junctions
1131   protects junctions from Snail-dependent disassembly. *J Cell Biol.* 212:219-229.
1132   Wolpert, L. 1969. Positional information and the spatial pattern of cellular differentiation. *J
1133   Theor Biol.* 25:1-47.
1134   Xie, S., and A.C. Martin. 2015. Intracellular signalling and intercellular coupling coordinate
1135   heterogeneous contractile events to facilitate tissue folding. *Nat Commun.* 6:7161.
1136   Yevick, H.G., P.W. Miller, J. Dunkel, and A.C. Martin. 2019. Structural Redundancy in
1137   Supracellular Actomyosin Networks Enables Robust Tissue Folding. *Dev Cell.*
1138   50:586-598.

1139

1140